The Astrophysical Journal, 910:73 (25pp), 2021 March 20 https://doi.org/10.3847/1538-4357/abd543

Green Bank Telescope Observations of ^{3}He$^+$: Planetary Nebulae

T. M. Bania[1] and Dana S. Balser[2]

[1] Institute for Astrophysical Research, Astronomy Department, Boston University, 725 Commonwealth Ave., Boston, MA 02215, USA; bania@bu.edu, dbalser@nrao.edu

[2] National Radio Astronomy Observatory, 520 Edgemont Rd., Charlottesville, VA 22903, USA

Received 2020 November 13; revised 2020 December 14; accepted 2020 December 18; published 2021 March 26

Abstract

We use the Green Bank Telescope to search for ^{3}He$^+$ emission from a sample of four Galactic planetary nebulae: NGC 3242, NGC 6543, NGC 6826, and NGC 7009. During the era of primordial nucleosynthesis, the light elements ^{2}H, ^{3}He, ^{4}He, and ^{7}Li were produced in significant amounts, and these abundances have since been modified primarily by stars. Observations of ^{3}He$^+$ in H II regions located throughout the Milky Way disk reveal very little variation in the ^{3}He/H abundance ratio—the "^{3}He Plateau"—indicating that the net effect of ^{3}He production in stars is negligible. This is in contrast to much higher ^{3}He/H abundance ratios reported for some planetary nebulae. This discrepancy is known as the "^{3}He Problem." We use radio recombination lines observed simultaneously with the ^{3}He$^+$ transition to make a robust assessment of the spectral sensitivity that these observations achieve. We detect spectral lines at ∼1–2 mK intensities, but at these levels, instrumental effects compromise our ability to measure accurate spectral line parameters. We do not confirm reports of previous detections of ^{3}He$^+$ in NGC 3242 nor do we detect ^{3}He$^+$ emission from any of our sources. This result calls into question all reported detections of ^{3}He$^+$ emission from any planetary nebula. The ^{3}He/H abundance upper limit we derive here for NGC 3242 is inconsistent with standard stellar production of ^{3}He and thus requires that some type of extra-mixing process operates in low-mass stars.

Unified Astronomy Thesaurus concepts: Stellar nucleosynthesis (1616); Galaxy chemical evolution (580); Planetary nebulae (1249)

1. The ^{3}He Problem

The ^{3}He abundance in Milky Way sources provides important constraints for many fields of astrophysics including cosmology, stellar evolution, and Galactic chemical evolution. The abundance of ^{3}He is derived from measurements of the hyperfine transition of ^{3}He$^+$, which has a rest wavelength of 3.46 cm (8.665 GHz). The present ^{3}He abundance results from a combination of big bang nucleosynthesis (BBN) and stellar nucleosynthesis (see, e.g., Wilson & Rood 1994). Abundances derived for the light elements ^{2}H, ^{3}He, ^{4}He, and ^{7}Li can be compared with BBN models for their primordial production to give an estimate for the primordial baryon to photon ratio, η. Observations made by the Wilkinson Microwave Anisotropy Probe (WMAP) also yield a value for η. The concordance of these values for η is a triumph of observational cosmology. Together, these analyses derive a ^{3}He primordial abundance of $(^3\mathrm{He/H})_\mathrm{p} = (1.00 \pm 0.07) \times 10^{-5}$ by number (Bania et al. 2002; Romano et al. 2003; Cyburt 2004). Subsequent to the BBN era, this primordial ^{3}He abundance will be modified by nuclear processing in many generations of stars.

We are studying the evolution of the ^{3}He abundance over cosmic time by using observations of ^{3}He$^+$ emission to derive the ^{3}He abundance in Milky Way H II regions and planetary nebulae (PNe). H II regions are zero-age objects compared to the age of the Galaxy. Their ^{3}He abundances chronicle the results of billions of years of Galactic chemical evolution (GCE). PNe abundances arise from material that has been ejected from low-mass ($M \lesssim 2\ M_\odot$) and intermediate-mass ($M \sim 2$–$5\ M_\odot$) stars. Standard stellar evolution models[3] predict the production of significant amounts of ^{3}He in low-mass stars with peak abundances of ^{3}He/H ∼ few $\times 10^{-3}$ by number (Iben 1967a, 1967b; Rood 1972). As the star ascends the red giant (RGB) and asymptotic giant (AGB) branches, the convective zone subsumes the ^{3}He-enriched material, which is expected to be expelled into the interstellar medium (ISM) via ejected planetary nebula shells (see, e.g., Faulkner 1970).

Rood et al. (1976, hereafter RST) first identified the interstellar ^{3}He abundance as being a significant constraint on stellar evolution models. Using yields from standard stellar models, RST found a ^{3}He enrichment of the primordial abundance due to stellar processing. The ^{3}He/H abundance in the ISM is thus an important GCE diagnostic. RST argued that standard stellar nucleosynthesis in low-mass stars predicts that: (1) the protosolar ^{3}He/H abundance should be less than that found in the present ISM, (2) the ^{3}He/H abundance should grow with source metallicity, and (3) there should be a ^{3}He/H abundance gradient across the Galactic disk with the largest abundances occurring in the highly processed inner Galaxy. None of these predictions is confirmed by observations.

H II regions sample the result of the chemical evolution of the Milky Way since its formation. After 40 yr of effort (see our papers starting and ending with Rood et al. 1979; Balser & Bania 2018a), our observations still yield ^{3}He abundances for H II regions that are inconsistent with RST's expectations. Furthermore, the H II region ^{3}He/H abundances together with those derived for protosolar material (Geiss 1993) and the local solar neighborhood (Gloeckler & Geiss 1996) all indicate a value for ^{3}He/H $\sim 2 \times 10^{-5}$ by number. H II region abundances thus show no evidence for stellar ^{3}He enrichment during the last 4.5 Gyr. Furthermore, there is no large ^{3}He abundance gradient across the Milky Way disk and, finally, there is no trend of ^{3}He abundance with source metallicity ("The ^{3}He Plateau").

---

[3] That is, models that only consider convection as a mixing mechanism in stellar interiors.

Nonetheless, there are three PNe with published ^{3}He$^+$ detections: NGC 3242 (Rood et al. 1992; Balser et al. 1997, 1999b), J 320 (Balser et al. 2006), and IC 418 (Guzman-Ramirez et al. 2016). The ^{3}He/H abundance ratios derived for these detections range from 2×10^{-4} to 6×10^{-3} by number, consistent with the yields predicted by standard stellar evolution models (e.g., Rood 1972). Furthermore, these abundances are an order of magnitude higher than the abundances found in H II regions (see, e.g. Balser & Bania 2018a). Thus, although some PNe have apparently produced ^{3}He according to standard stellar nucleosynthetic expectations, there is no evidence for substantial ^{3}He enrichment in the Milky Way ISM. This conundrum has long been dubbed "The ^{3}He Problem" (Galli et al. 1995).

Rood et al. (1984, RBW hereafter) suggested that the ^{3}He problem could be related to striking chemical abundance anomalies in red giant stars. They posited that some extra-mixing process during the RGB stage in stellar interiors might reduce the ^{3}He abundance, and this might also explain the depletion of ^{7}Li in main-sequence stars and the low ^{12}C/^{13}C abundance ratios in low-mass RGB stars (also see Charbonnel 1995).

Resolving "The ^{3}He Problem" requires that the vast majority of low-mass stars fail to enrich the ISM with ^{3}He produced during their nucleosynthetic lifetimes. GCE models can account for "The ^{3}He Plateau" only if $\gtrsim$90% of solar analog stars are nonproducers of ^{3}He (Galli et al. 1997; Tosi 1998; Palla et al. 2000; Chiappini et al. 2002). Exactly what produces this extra-mixing has been actively investigated for many years. Balser & Bania (2018a) give a comprehensive review of the various physical mechanisms proposed and the current status of this research. The most significant recent advance was made by Charbonnel & Zahn (2007b), who argue that the thermohaline instability, a double-diffusive instability, is an important mechanism. The best stellar evolutionary models for low- and intermediate-mass stars now include both the thermohaline instability and rotation-induced mixing (Charbonnel & Lagarde 2010; Lagarde et al. 2011). Lagarde et al. (2012) used their model ^{3}He yields together with GCE models to predict a modest enrichment of ^{3}He with time and ^{3}He/H abundance ratios about a factor of 2 higher in the central regions of the Milky Way relative to the outer regions.

The scatter of the ^{3}He Plateau abundances determined by Bania et al. (2002), however, is large and spans the range of abundances predicted by Lagarde et al. (2012). Balser & Bania (2018a) improved the derived ^{3}He/H abundances for Galactic H II regions by studying a sample of five morphologically simple nebulae located over a wide range of Galactocentric radii: 4.4 kpc $< R_{\rm gal} <$ 16.2 kpc. Their goal was to derive accurate ^{3}He/H abundance ratios for a small sample of sources to uncover any trend in the ^{3}He/H abundance with $R_{\rm gal}$ and to compare their results with the predictions of Lagarde et al. (2012).

Balser & Bania (2018a) determined a shallow ^{3}He/H radial gradient of $-0.116 \pm 0.022 \times 10^{-5}$ kpc^{-1}, consistent with the overall trend predicted by Lagarde et al. (2012). Their ^{3}He/H abundance ratios, however, are typically slightly less than the models that include thermohaline mixing. Furthermore, Balser & Bania (2018a) could not obtain ^{3}He/H abundances with sufficient accuracy to determine whether or not strong magnetic fields in some stars could inhibit the thermohaline instability as predicted by Charbonnel & Zahn (2007a).

A critical constraint on all these stellar evolution models, however, is the ^{3}He/H abundance derived for a sample of just three PNe. Observations of ^{3}He$^+$ emission are very challenging. Accurate measurement of these weak, broad spectral lines requires significant integration time and a stable, well-behaved spectrometer (Balser et al. 1994). This is particularly true when observing ^{3}He$^+$ emission from PNe because the lines are weaker and broader than for H II regions.

Our goal here is to confirm our previous ^{3}He$^+$ detection for NGC 3242 and to derive accurate ^{3}He/H abundance ratios for it and a small sample of other PNe. The Green Bank Observatory's (GBO)[4] Green Bank Telescope (GBT) *X*-band (3 cm wavelength) spectrometer is in principle an order of magnitude more sensitive than any previous centimeter-wavelength radio frequency telescope/spectrometer system. This increased sensitivity results from the GBT's unique 100 m clear aperture, unblocked optics that enable unprecedented dynamic range measurements together with its *X*-band receiver, and autocorrelation spectrometer (ACS).

2. The Planetary Nebula Sample

We are observing a sample of PNe that is purposefully biased to maximize the likelihood of detecting ^{3}He$^+$ emission (see, e.g., Balser et al. 1999a). Our PN targets are sources that both show evidence for no extra-mixing and also have physical properties that, for a given ^{3}He/H abundance, would produce the largest ^{3}He$^+$ intensities. We have chosen PN targets based on their estimated ^{3}He$^+$ intensity using an assumed constant ^{3}He/H abundance together with the following criteria: (1) Sources with the strongest expected ^{3}He$^+$ intensities. This requires measurements of PN brightness, angular size, and distance. Ordinarily, the radio continuum was used to estimate the brightness. (2) Sources that are located $\gtrsim$500 pc away from the Galactic plane. This increases the likelihood that a given PN is drawn from the old/thick disk or halo population. On average, such PNe would have low progenitor masses, longer main-sequence lifetimes, and, thus, higher ^{3}He/H abundances. (3) Sources without any indication in the nebular gas of nuclear processing on the RGB or AGB. High He, N, or ^{13}C abundances would suggest that the gas had undergone CNO processing and, presumably, ^{3}He depletion. (4) Sources where most of the He is singly ionized.

Here, we used the GBT to search for ^{3}He$^+$ emission from four Galactic PNe: NGC 3242, NGC 6543, NGC 6826, and NGC 7009. Table 1 summarizes properties of our PN sample. Listed are the source name, equatorial coordinates, optical heliocentric source velocity, $V_{\rm opt}$, heliocentric distance, $D_{\rm sun}$, and the effective temperature of the central exciting star, $T_{\rm eff}$. The $D_{\rm sun}$ values are Gaia DR2 parallax distances from Schönberner & Steffen (2019). The effective temperatures stem from Schönberner et al. (2018).

We have previously reported detections of ^{3}He$^+$ emission from NGC 3242 using independent observations made with the Max Planck Institut für Radioastronomie (MPIfR) 100 m and the National Radio Astronomy Observatory (NRAO) 140 Foot telescopes. Moreover, the composite ^{3}He$^+$ 100 m spectrum of NGC 6543+NGC 7009 suggests ^{3}He$^+$ emission at the ~1 mK intensity level. Also, observations made with the Arecibo 305 m telescope give a composite PNe spectrum including

---

[4] The Green Bank Observatory and National Radio Astronomy Observatory are facilities of the National Science Foundation operated under cooperative agreements by Associated Universities, Inc.

Table 1
Galactic Planetary Nebula Sample

Source	R.A. (J2000) (hh:mm:ss.s)	Decl. (J2000) (dd:mm:ss)	$V_{\rm opt}$[a] (km s^{-1})	$D_{\rm sun}$[b] (kpc)	$T_{\rm eff}$[c] (K)
NGC 3242	10:24:46.2	-18:38:34	$+4.6$	$1.466^{+0.219}_{-0.168}$	90,000
NGC 6543	17:58:33.4	$+66$:37:59	-66.1	$1.625^{+0.212}_{-0.167}$	68,000
NGC 6826	19:44:48.3	$+50$:31:30	-6.2	$1.575^{+0.128}_{-0.103}$	46,000
NGC 7009	21:04:10.8	-11:21:57	-46.6	$1.154^{+0.177}_{-0.136}$	82,000

Notes.

[a] Heliocentric radial velocity using the optical definition of velocity and the barycentric reference frame (Greisen et al. 2006).

[b] Gaia DR2 parallax from Schönberner & Steffen (2019).

[c] Effective temperature of central exciting star from Table 8 in Schönberner et al. (2018).

NGC 6543 that showed a hint of ^{3}He$^+$ emission at this same level (Bania et al. 2007).

Our sample PNe are shown in Figure 1 where images of the PN cores have been overlaid atop more sensitive wide-field images of the PN halos produced by thousands of years of AGB winds injecting gas into the surrounding nebula at 10–15 km s^{-1}. Notable and oddly, each of the cores in these four PNe contains pairs of small, [N II]-emitting regions—"Fast Low-ionization Emission Regions" (FLIERs)—seen as red knots on opposite sides of the central star. FLIERs are volumes of gas moving at supersonic outflow speeds that are significantly higher than the nebular flows in which they are embedded, and their ionizations are much lower. In general, FLIERs are rare, so the ubiquitous presence of FLIERS in all four of our targets is somewhat surprising.

All of our PNe are surrounded by extended low-density halos that are expanding due to episodic mass loss from their evolved stellar cores. An AGB star steadily blows off its outer layers. After this, although the mass-loss rate from the faster post-AGB outflows is higher than that carried by the AGB winds, the duration of this mass ejection is quite brief compared to the AGB ejection phase. Because of this, at the end of its evolution, nearly all of the mass of a PN is ejected by the slow AGB winds and this material ultimately ends up residing in its halo.

Our GBT observations measure the combined emission from the entire core + halo complex of our sample PNe. The angular resolution (the half-power beamwidth, HPBW) of the GBT at 8665 GHz is plotted in Figure 1 as a yellow circle in these ~180″ square images. Because these PN core radii are typically ~10″ in size, approximately 80% of the Gaussian GBT beam area is sampling only halo gas.

3. GBT Observations and Data Analysis

We used the GBT to search for ^{3}He$^+$ emission from our PN sample during a series of observing sessions held between 2004 and 2011. These measurements targeted both PNe and H II regions. Here we focus on our PNe sample; Balser & Bania (2018a) analyzed the H II regions and discussed the implications of their derived ^{3}He abundances. Observations were made with the *X*-band (8–10 GHz) receiver and either the Digital Continuum Receiver (DCR) or ACS backend. Before 2011, we targeted all four PNe in our sample and used a slightly different tuning configuration of the ACS than that employed during the 2011 epoch. In 2011, we only observed NGC 3242 and NGC 6543. This results in significantly larger total integration times for the ^{3}He$^+$ and radio recombination line (RRL) spectra for these two nebulae compared with those measured for NGC 6826 and NGC 7009. Full details for the 2011 observations, tuning configuration, and data analysis strategy are described by Balser & Bania (2018a).

3.1. Observing Protocol and Calibration

During each observing session, the pointing and focus were updated every ~2 hr using DCR observations of the continuum emission from a calibration source located within ~ 15° of the target position. To calibrate the antenna temperature intensity scale, a noise signal with an intensity of ~5%–10% of the total system temperature, $T_{\rm sys}$, was injected into the signal path. For the GBT *X*-band system, these noise diodes have intensities $T_{\rm cal} \sim 2$ K. To check the flux density calibration, we observed the continuum emission from the flux density calibrator 3C 286. We adopt the Peng et al. (2000) flux density for 3C 286 and assume a telescope gain at *X* band of 2 K Jy^{-1} (Gigho et al. 2001). Based on these measurements, we deem the intensity scale to be accurate to within ~5%–10%.

3.2. Radio Continuum Emission

The continuum emission from PNe stems from thermal free–free bremsstrahlung radiation from the nebular plasmas. Since hydrogen is overwhelmingly the most abundant element in these plasmas, analyzing the continuum emission allows one to determine the PNe hydrogen abundances. Hydrogen abundances are essential for the derivation of the ^{3}He/H ratio.

We measured the continuum emission properties of our PN sources with the GBT using the DCR tuned to a rest frequency of 8665 MHz. The continuum emission intensity was sampled over a bandwidth of 320 MHz as the GBT was slewed in a cross pattern—first in R.A. and then in decl.—centered at each PN position. Table 2 summarizes Gaussian fits to these measurements. Listed are the peak intensities and angular sizes in each direction together with $\pm 1\sigma$ errors in the fits.

3.3. Radio Recombination Line Emission

To acquire our spectral line observations, we employ total power position switching by observing an Off-source position for 6 minutes and then the target On-source position for 6 minutes, for a total time of 12 minutes. The Off position is offset 6 minutes in R.A. relative to the On position so that the telescope tracks the same sky path during each observation.

Each total power Off/On pair produces 16 independent spectra that are observed simultaneously. For all our observations, the

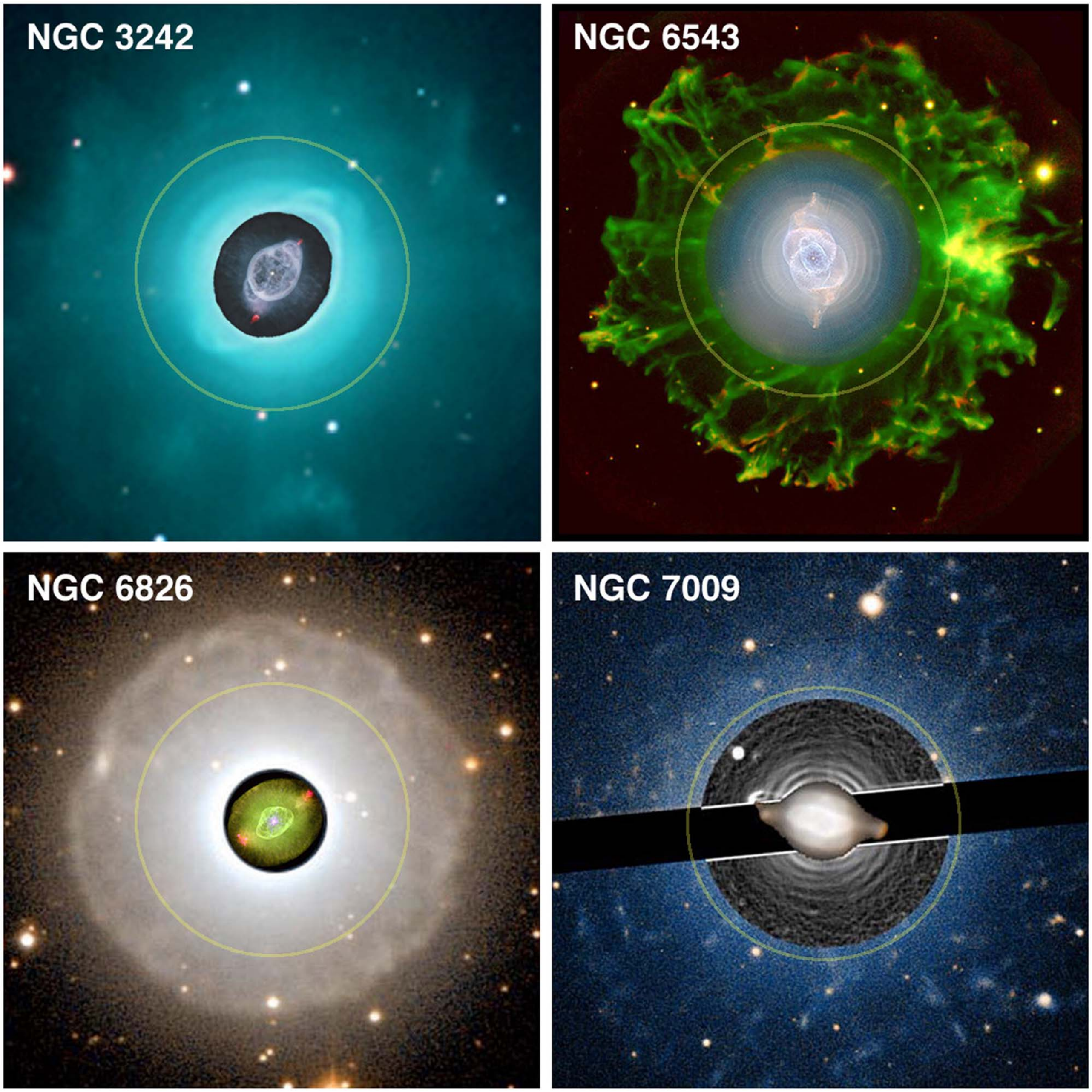

Figure 1. Public domain optical images of the planetary nebulae studied here. North is up in each ∼180″ square image. The yellow circles are centered on the exciting stars and show the GBT beam size. Images of the PN cores have been overlaid atop more sensitive wide-field images of the PN halos. The halos shown here are photometrically uncalibrated ground-based images, and the optical filters vary from one object to another. Furthermore, in order to make the halos visible, their images have been intensity flattened so what is seen here is the logarithm of the surface brightness. Ramos-Larios et al. (2016) describe the general properties of faint optical rings in PNe.

Table 2
Continuum Emission Properties at 8665 MHz

Source	T_α[a] (K)	Θ_α[b] (arcsec)	T_δ[a] (K)	Θ_δ[b] (arcsec)
NGC 3242	1.25 ± 0.01	85.8 ± 0.9	1.24 ± 0.01	91.6 ± 0.8
NGC 6543	1.41 ± 0.01	85.5 ± 0.3	1.43 ± 0.01	84.2 ± 0.5
NGC 6826	0.65 ± 0.01	87.7 ± 0.8	0.66 ± 0.01	88.7 ± 0.8
NGC 7009	1.08 ± 0.01	84.3 ± 0.9	1.08 ± 0.01	83.5 ± 0.9

Notes.
[a] R.A. and decl. intensities in antenna temperature units.
[b] R.A. and decl. FWHM angular sizes.

GBT ACS spectrometer is configured with eight spectral windows (SPWs) at two orthogonal, circular polarizations for a total of 16 SPWs. Each SPW has a bandwidth of 50 MHz spanning 4096 spectral channels. This gives a spectral resolution per channel of 12.2 kHz, or a velocity resolution of 0.42 km s^{-1} at 8665.65 MHz. The eight SPWs were tuned to different center frequencies in order to observe both ^{3}He$^+$ and also a host of different RRL transitions that are used to assess spectrometer performance. For all our observations, six of the eight SPW tunings were identical. The 2011 epoch observations replaced two RRL transition SPWs with ^{3}He$^+$ tunings displaced in frequency (see below).

There is a plethora of RRL transitions that lie within the frequency ranges of our observed SPWs. These are compiled in

Table 3
RRL Transitions[a]

ΔN	H^+ He^+ C^+
1	91α 92α
2	114β 115β
3	130γ 131γ 132γ
4	144δ 145δ
5	152ϵ 154ϵ 155ϵ 156ϵ
6	164ζ 165ζ
7	171η
8	179θ 180θ 181θ
9	186ι 187ι 188ι
10	190κ 193κ
11	198λ 199λ
12	201μ 203μ 206μ
13	206ν 208ν 210ν $^*238\nu$
14	211ξ 213ξ 215ξ
15	$221o$
16	220π 222π 224π
17	222ρ 224ρ 227ρ 228ρ 230ρ
18	228σ 231σ 232σ 234σ
19	232τ $^*234\tau$ 235τ 236τ 238τ
20	238υ
21	239ϕ 242ϕ
22	245χ 247χ 249χ
23	249ψ
24	249ω

Notes. All these recombination line transitions lie within the spectral windows observed. Transitions with $\Delta N > 7$ are too weak to be detected with the sensitivity achieved here.

[a] Transitions with $N > 250$ or $\Delta N > 25$ not listed. Not all transitions for all ionic species were detected.

Table 3 for transitions with principal quantum numbers $N < 250$ that have quantum number changes $\Delta N < 25$. We list these RRLs for completeness; transitions with $\Delta N > 7$ are too weak to be detected with the sensitivity achieved by the observations reported here.

The data were analyzed using the single-dish software package TMBIDL[5] (Bania et al. 2016). Before averaging, each Off/On pair spectrum was visually inspected and discarded if significant spectral baseline structure or radio frequency interference (RFI) was present. Narrowband RFI that did not contaminate the spectral lines was excised and the RFI-cleaned spectrum was included in the average. Spectra were averaged in different ways to assess any problems with the spectral baselines. For example, we made the following tests: (1) inspected the average spectrum for each observing epoch to search for any anomalies; (2) divided the entire data set into several subsets to assess whether the noise was integrating down as expected; (3) compared the two orthogonal polarizations, which should have nearly identical spectra; and (4) compared the different SPWs for cases where we had simultaneous, duplicate $^3He^+$ and RRL transition tunings (see Section 4).

The GBT observations reported here are very deep integrations. The total integration time for NGC 3242 and NGC 6543 spectra is ~300 hr; for NGC 6826 and NGC 7009, it is ~50 hr. This gives typical rms noise after smoothing to 5 km s^{-1} resolution of ~0.2 mK and ~0.5 mK, respectively. Integration times for different SPW tunings vary depending on the ACS configuration for a particular observing epoch and on how much data were excised during the averaging process.

To improve spectral sensitivity, each spectrum was smoothed to a velocity resolution of 5 km s^{-1}. Any sky continuum emission and baseline frequency structure was then removed by fitting a fifth-order baseline model that was then subtracted. We explored using different order baseline fits and determined that fifth order was the best compromise between under and overfitting. A clear indication of overfitting, for example, would be to achieve an impossible spectral rms for the integration time. The RRL properties were measured by fitting a Gaussian function to the spectra using a Levenberg–Markwardt (Markwardt 2009) least-squares method to derive the peak intensity and the FWHM line width. As we shall show below, these measurements of RRL properties make astrophysical sense and so indicate that we have not overfitted the removal of the instrumental baselines.

The H91α, H114β, and H131γ spectra analyzed in this way are shown for our PN sample in Figures 2 and 3, respectively. Each spectrum is a 12.5 MHz wide subset of its native 50 MHz bandwidth SPW. The RRL parameters measured for our PN sources are given in Appendix A for all RRL transitions detected at $\gtrsim 3\sigma$ level. Compiled there for each nebula is the RRL transition, the change in principal quantum number, ΔN, the line intensity, T_L in mK, and FWHM line width, ΔV in km s^{-1}, together with the rms noise in mK and total integration time, $t_{\rm intg}$ in hr, of the spectral band containing the transition. Also listed are the 1σ errors of the Gaussian fits to the intensity, σT_L, and line width, $\sigma\Delta V$.

3.4. $^3He^+$ Emission

Detecting $^3He^+$ emission from PNe turns out to be very challenging. These emission lines are weaker and broader than those produced by H II regions. The $^3He^+$ spectra for our PN sample are shown in Figure 4. As for the RRL analysis, these spectra were smoothed to a 5 km s^{-1} velocity resolution, and a fifth-order polynomial instrumental baseline model was subtracted from the data. Each PN in Figure 4 has two spectra shown. The top panel displays the baseline model atop the smoothed spectrum, and the bottom panel plots the spectrum after this baseline model is subtracted.

We judge that we have not robustly detected $^3He^+$ emission from any of our target PNe. The spectra show that any $^3He^+$ signal must have an intensity less than 1 mK. Upper limits for $^3He^+$ emission from our sample PNe are listed in Table 4. For NGC 3242 and NGC 6543, we can fit Gaussian functions to their spectra to provide the upper limits. These fits give 2.6σ and 4.3σ $^3He^+$ emission features for NGC 3242 and NGC 6543, respectively. For NGC 6826 and NGC 7009, no realistic fits could be made so their upper limits are three times their rms spectral noise.

Our RRL analysis in Section 4 below indicates that, due to instrumentally caused frequency structure in the baselines, spectral line parameters at $\lesssim 1$ mK level cannot be measured accurately with the sensitivity achieved by these GBT observations. We explored using different baseline model fitting regions and polynomial orders in analyzing these $^3He^+$ spectra. We can make the $^3He^+$ feature stronger, but only at the expense of creating nonphysical H171η line parameters. The spectra in Figure 4 all use the same fitting regions to model the

---

[5] Version 8.1; see https://github.com/tvwenger/tmbidl.

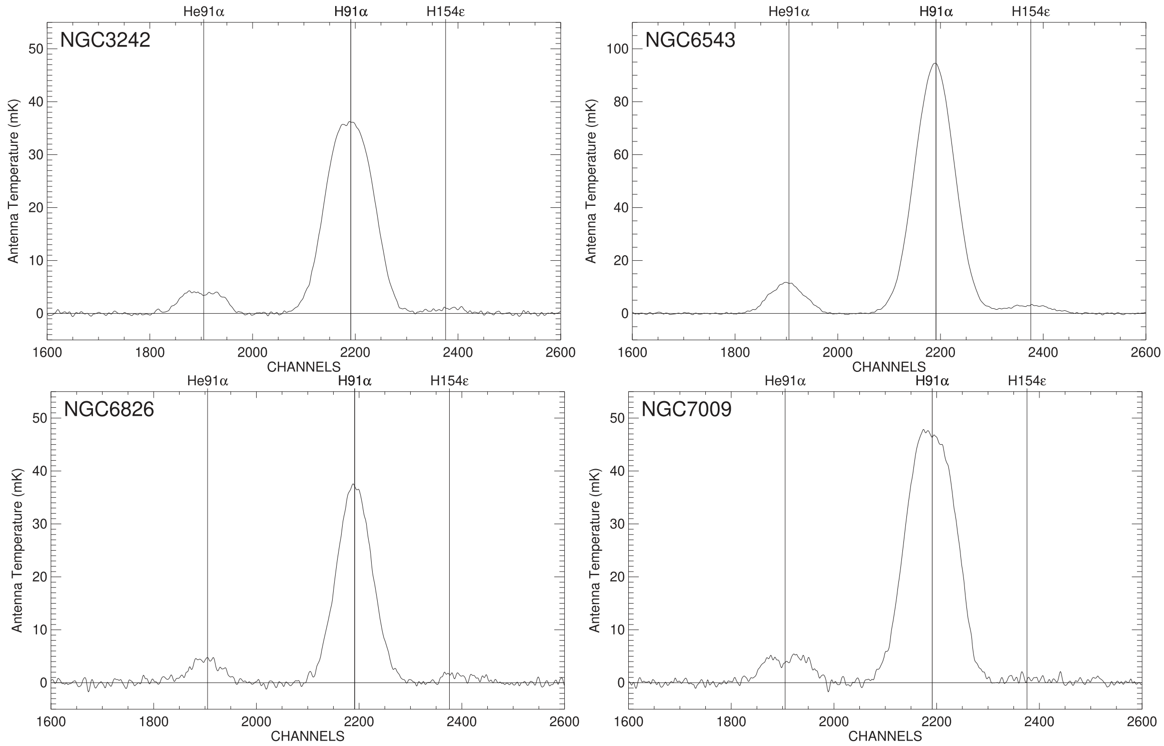

Figure 2. Observed H91α spectra for the planetary nebula sample. Shown clockwise starting from top left, they are NGC 3242, NGC 6543, NGC 7009, and NGC 6826. Vertical lines flag, from left to right, the recombination line transitions: He91α, H91α, and H154ϵ. Each spectrum spans a total bandwidth of 12.5 MHz. The spectra have been smoothed to a velocity resolution 5 km s^{-1} and a fifth-order model for the instrumental baseline has been subtracted.

instrumental baselines. These baseline models, however, do not entirely remove instrumental baseline frequency structure. That the noise in the NGC 3242 ~300 hr spectrum is larger than that in the ~250 hr NGC 6543 spectrum makes it clear that such structure still remains in these spectra. This is why we are only quoting upper limits for ^{3}He$^+$ emission from these observations.

4. Instrumental Frequency Structure in GBT Spectral Baselines

Instrumental effects limit the spectral sensitivity of most single-dish radio telescopes. These effects cause frequency structure in spectra that can mimic real emission lines. For traditionally designed single-dish radio telescopes, this frequency structure in spectral baselines is primarily caused by reflections from the superstructure. The GBT was specially designed with a clear aperture to significantly reduce reflections from the secondary structure and therefore improve the image fidelity and spectral purity. Nevertheless, baseline structure still, unfortunately, exists and is primarily located within the electronics (Fisher et al. 2003).[6] The GBT *X*-band (3 cm wavelength) receiver is a heterodyne system wherein radio waves from the sky are mixed with a local oscillator to convert the signal to an intermediate frequency (IF). Unfortunately, the GBT IF system transports analog signals over a ~1 mile long path length. There are a host of electronic components in this path, and each can produce reflections and, therefore, standing waves. The spectral baselines are significantly better for the GBT than for traditionally designed, on-axis telescopes but they are still the limiting factor in measuring accurate line parameters for weak, broad spectral lines.

For observing epochs starting in 2011 and later, we used the strategy described by Balser & Bania (2018a) to mitigate instrumental frequency structure in the GBT IF system. This technique simultaneously tunes four SPWs to the ^{3}He$^+$ transition with center frequencies offset by 0, 3, 6, and 9 MHz during data acquisition. The idea is to move the ^{3}He$^+$ transition around in IF frequency space and that when the four SPWs are subsequently aligned and averaged, the result smooths out instrumental frequency structure in the IF. Balser & Bania (2018a) evaluated the efficacy of this technique. These baseline structure tests are germane here because measurements of our planetary nebula and H II region targets were interleaved during all observing epochs.

An important test was to observe two extragalactic calibration sources, the quasars 3C 286 and 3C 84, which have 9 GHz continuum antenna temperatures of 10 K and 50 K, respectively. The advantage of using these extragalactic sources is that they do not have any measurable spectral lines at these frequencies. The observing procedures and ACS configuration were the same as the observations for the H II region and PN targets.

These bright calibrators were chosen to amplify any instrumental spectral artifacts. The instrumental baseline structure for these quasar observations is therefore expected to be much worse than for our PNe target sources which have continuum antenna temperatures $\lesssim$1.5 K (see Table 2). Balser & Bania (2018a) show that the spectral baselines produced by this frequency offset observing technique are clearly flatter. Moreover, the amplitude of the remaining baseline features roughly scales with continuum intensity most likely due to the

---

[6] See http://library.nrao.edu/public/memos/edir/EDIR_312.pdf.

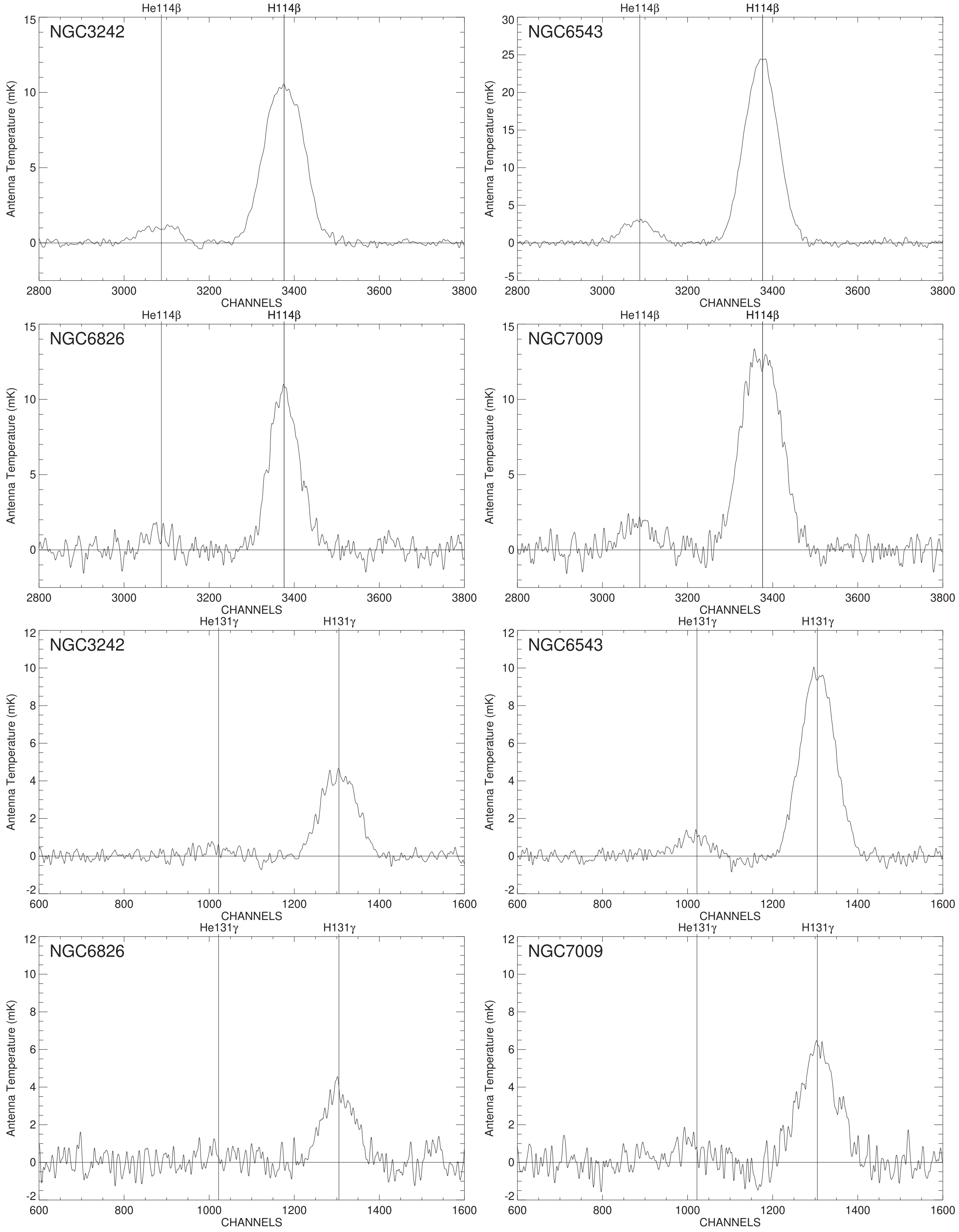

Figure 3. Observed H114β and H131γ spectra and for the planetary nebula sample. Each spectrum spans a total bandwidth of 12.5 MHz. The spectra have been smoothed to a velocity resolution of 5 km s^{-1} and a fifth-order model for the instrumental baseline has been subtracted. For the 114β spectra, vertical lines flag, from left to right, the recombination line transitions: He114β and H114β. For the 131γ spectra, vertical lines flag, from left to right, the recombination line transitions: He131γ and H131γ.

power mismatch between the On- and Off-source observations. Averaging over the four frequency offset ^{3}He$^+$ SPWs does not reduce the random thermal noise because the signals are correlated, but the instrumental systematic noise is reduced. The improvement is, however, not dramatic. Careful scrutiny of early-epoch data acquired without using this technique gave us no reason not to include these data in the final averages.

A major goal here is to assess the instrumental baseline frequency structure that remains in our PN data. These systematic effects, and not random Gaussian rms noise, limit the spectral sensitivity that we can achieve with the GBT/ACS spectrometer system. We thus distinguish between thermal radiometer noise, "RN," and systematic instrumental baseline noise, "BN." A radio spectrometer's rms thermal noise should obey the radiometer

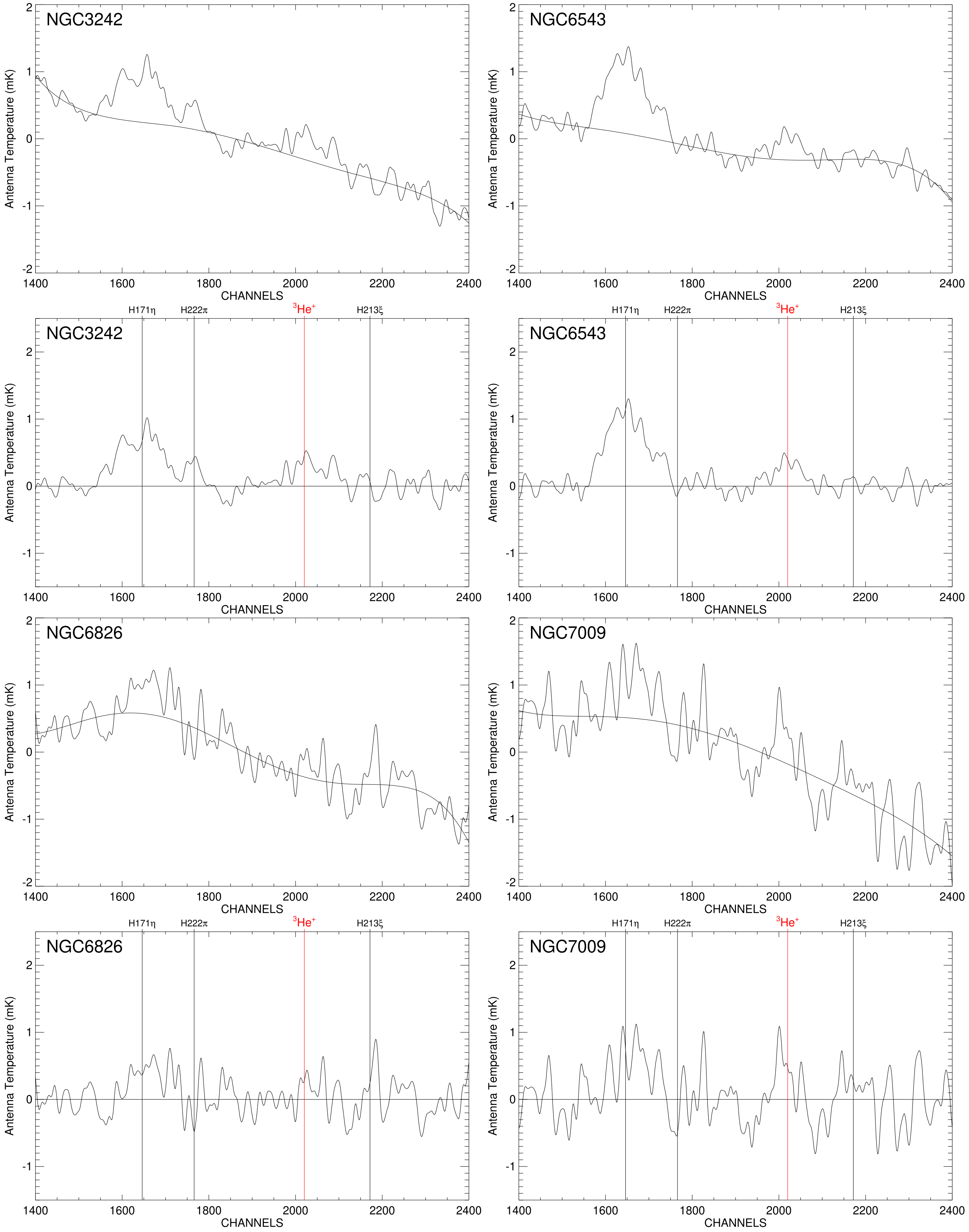

Figure 4. ^{3}He^{+} spectra for the planetary nebula sample. Top panels: the average spectrum smoothed to a 5 km s^{-1} velocity resolution with the fifth-order model fit to the instrumental baseline superimposed. Bottom panels: the spectrum after the baseline model is subtracted. Vertical lines flag, from left to right, the H171η, H222π, ^{3}He^{+}, and H213ξ transitions.

equation; the rms of this RN should diminish as the square root of the integration time: rms $\propto t_{\rm intg}^{-1/2}$. Larger rms values for the same integration time are manifestations of instrumental baseline frequency structure—the BN. As we have done for all the ^{3}He^{+} experiment telescopes, we use the plethora of RRL measurements to assess the performance of the GBT/ACS spectrometer system.

Table 4
Upper Limits for $^{3}He^{+}$ Emission from Planetary Nebulae

Source	T_L (mK)	σT_L (mK)	ΔV (km s^{-1})	$\sigma\Delta V$ (km s^{-1})	rms (mK)	t_{intg} (hr)
NGC 3242[a]	<0.36	0.02	48.0	2.94	0.145	301.7
NGC 6543[a]	<0.39	0.02	29.1	1.63	0.112	256.1
NGC 6826[b]	<0.77	...	...	...	0.257	51.4
NGC 7009[b]	<1.04	...	...	...	0.348	44.0

Notes.
[a] Upper limit derived from Gaussian fit to the $^{3}He^{+}$ spectrum.
[b] Upper limit is three times the rms noise listed here. This noise figure is calculated for the spectral regions used to model the instrumental baseline.

For example, the RRL line intensities should not vary with time, the $^{4}He^{+}/H^{+}$ abundance ratio should not be a function of the principal quantum number, and the lines should only be seen in emission. RRL theory predicts LTE line intensities, and these can be used to assess spectrometer performance. For any given nebula, the entire ensemble of RRLs should give an astrophysically self-consistent set of measured line parameters. Any deviations or inconsistencies are caused by instrumental effects which, experience shows, inevitably appear at some point as one attains ever-increasing sensitivity levels. At the sensitivity required by the ^{3}He experiment, characterizing the spectrometer's performance is an ongoing, evolving process.

A spectrometer that is behaving properly only has RN and so will obey the radiometer equation. Because the ACS spectral bandwidth and sampling mode are identical for all our observations, the radiometer equation demands that the rms noise in a spectrum should only depend on the system temperature, T_{sys}, and the integration time, t_{intg}: rms $\propto T_{sys}/\sqrt{t_{intg}}$. We therefore adopt the sensitivity metric, Q, used by Balser et al. (1994) to evaluate the performance of radio spectrometers where $Q = (\sqrt{t_{intg}} \times \text{rms})/T_{sys}$. Here, the rms is that measured for each spectrum.

A perfect radiometer would have a Q of unity, but the ACS is an autocorrelator and its sensitivity is less than this ideal performance. For our observations, the ACS uses nine-level sampling and uniform channel weighting. Thus, if the GBT/ACS spectrometer only has RN, it should have $Q_{ACS} = 1.63$ at 8665 GHz for a spectral resolution of 5 km s^{-1}. Furthermore, the spectral rms should integrate down with increased observing time, t_{intg}, and the Q value ought to remain constant at Q_{ACS}. If there is, however, systematic instrumental baseline structure, BN, then the spectrometer's Q value will be larger than Q_{ACS}. BN will also manifest itself in the dispersion of Q values for a given integration time. Finally, although RN will integrate down with increased observing time, BN will always be present so the spectral Q will always remain above Q_{ACS} and the dispersion of Q values will persist no matter how large t_{intg} gets.

The Q factors attained by our GBT observations are plotted in Figure 5 as a function of t_{intg}. Spectra for all our PNe targets and SPW tunings are contained in this plot. Included are not only all the spectra whose RRL properties are listed in Appendix A, but also temporal subsets of the measurements leading to these spectra together with composite spectra that stem from averages of two or more PNe for the same RRL transitions. These latter data are needed to provide a more complete sampling of t_{intg}.

For the spectral integration times achieved by our $^{3}He^{+}$ observations, Figure 5 shows that the GBT/ACS spectrometer's performance—characterized by its spectral Q factors—is independent of integration time. A linear fit to these data yields an essentially flat relationship between Q factor and integration time; the slope across Figure 5 is 0.00020 ± 0.00019. The average Q factor is $\langle Q\rangle = 1.62 \pm 0.20$ ($\pm 12.3\%$), which is nearly identical to the linear fit's intercept of 1.59 ± 0.03. Thus, Figure 5 demonstrates that the GBT/ACS spectrometer's random thermal rms noise—its RN—is integrating down as expected from the radiometer equation.

This average Q factor is, remarkably, essentially identical to the $Q_{ACS} = 1.63$ value expected for the ACS from pure radiometer noise. Nonetheless, the systematic instrumental BN frequency structure is manifested by the $\sim$12% dispersion in the Q factor present for any t_{intg} value. The spectra used to craft Figure 5 were all smoothed to a common velocity resolution of 5 km s^{-1}. These spectra, however, come from SPWs that sample different places in IF space. Each SPW is tuned to a different center frequency. Because of this, a 5 km s^{-1} velocity resolution results in slightly different frequency resolutions for the different SPWs and that will produce some variation in Q for a fixed T_{sys} and t_{intg}. Our ACS SPW tuning frequencies span the range from 8280 to 8918 MHz. This produces an expected $\sim$4% variation in Q from different SPW tunings assuming all else is the same. The measured variation of the average Q for our experiment is $\sim$3 times larger than this. This is due to BN: SPWs that stem from different places in IF space show different instrumental frequency structure.

Comparing measurements that ought to be identical provides another test of radiometer performance. Here we do this in two ways by using measurements of: (1) identical RRL transitions and (2) RRL transitions with the same ΔN but with different, but adjacent principal quantum numbers, N. The first type of measurements are RRL transitions with the same (N,ΔN) observed simultaneously but in different SPWs. These spectra sample different regions of IF and ACS baseband space and are thus subject to different BN. These transitions are labeled H114a/H114b (β lines; $\Delta N = 2$), H130a/H130b (γ lines; $\Delta N = 3$), and H144b/H144g (δ lines; $\Delta N = 4$) in Appendix A. The second class of test RRLs exploits the fact that at high N levels, the energy differences for ΔN transitions occurring from nearby N levels are nearly identical, provided that the N range is not too great. Thus, the RRL intensities for adjacent N transitions with the same ΔN, e.g. H114β/H115β, ought to be close to unity.

This comparison is made in Figure 6 using the RRL measurements listed in Appendix A. It plots the fractional ratio, $(W(N,\Delta N)/\langle W_{\Delta N}\rangle) - 1$, as a function of the transition principal quantum number, N, where $W(N,\Delta N)$ is the integrated intensity of an RRL transition in mK km s^{-1} and $\langle W_{\Delta N}\rangle$ is the average integrated intensity of all observed transitions with the same ΔN. We use the integrated intensity, $W = T_{pk} \times \Delta V_{FWHM}$, to better characterize the RRL measurement. Above the x-axis of Figure 6, we also plot the ΔN values of the RRL transitions. As is clear from this figure, our RRL plots with either N or ΔN x-axes are equivalent because N increases monotonically from $\Delta N = 1$, which for our data has $N = 91$, to $\Delta N = 7$, where $N = 171$ (see Table 3). When interpreting the information presented in Figure 6, it is important to keep in mind that the top panel PNe sources, NGC 3242 and NGC 6543, have integration times between $\sim$250 and $\sim$300 hr whereas the

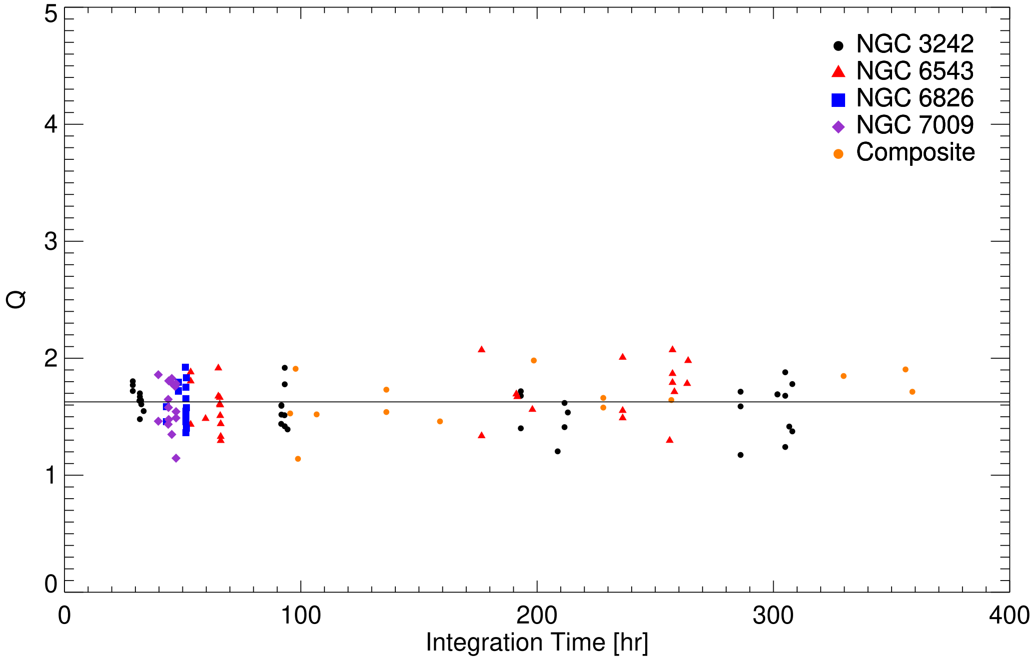

Figure 5. The GBT/ACS spectrometer system performance for this experiment. Shown is the sensitivity metric Q (see text) plotted as a function of total integration time for various subsets of the RRL data for our PN sample sources. "Composite" spectra stem from averages of two or more PNe. These Q values do not change with integration time as they should. The horizontal solid line marks the data average: $Q = 1.62$.

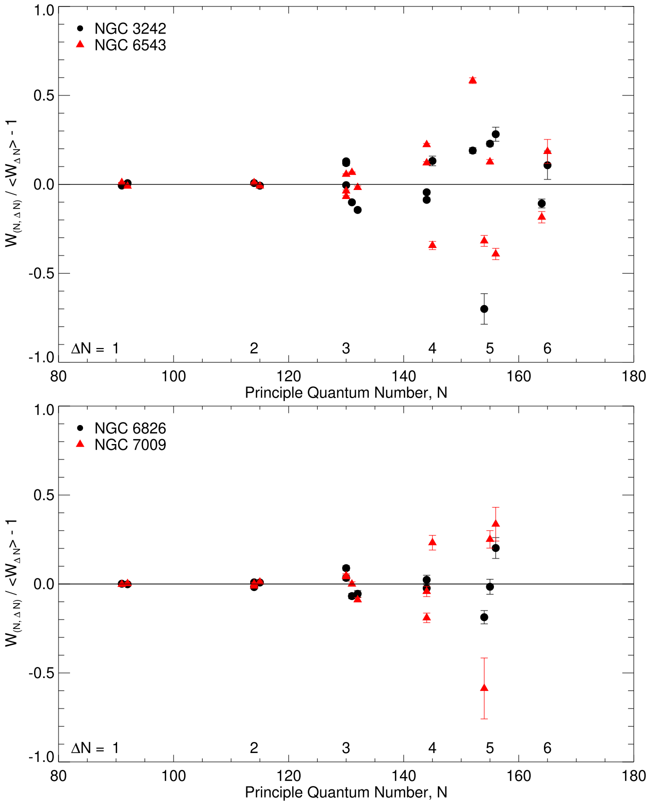

Figure 6. Comparison of measured RRL parameters for transitions with either the same (N,ΔN) or the same ΔN with different, but adjacent N values. The ratio of the integrated intensity of an RRL transition, $W(N,\Delta N)$ (mK km s^{-1}), and $\langle W_{\Delta N}\rangle$, the average integrated intensity of all observed transitions with the same ΔN, is plotted fractionally, $(W(N,\Delta N)/\langle W_{\Delta N}\rangle) - 1$, as a function of the transition principal quantum number, N. The ΔN of the transitions is also shown above the x-axis. At these high-N levels, transitions with nearby N values emit, to first order, spectral lines with the same intensities.

bottom panel targets, NGC 6826 and NGC 7009, have much smaller, ~ 50 hr, integration times.

The RRL comparisons in Figure 6 show that for the α ($\Delta N = 1$) and β ($\Delta N = 2$) transitions our integrated intensity measurements agree to within $\lesssim$1% for all our PN targets. These RRLs have the largest intensities; the weaker β line intensities span ~10 to ~25 mK for our sample PNe. For γ ($\Delta N = 3$) transitions, the comparison shows poorer agreement and higher-order ΔN transitions evince a large dispersion in the measured integrated intensities. For $\Delta N > 3$ transitions, the W ratio discrepancies exceed our ~10% intensity scale calibration uncertainty, reaching differences as large as ~30%. The magnitude of these discrepancies are a manifestation of BN at the ~2 mK level.

Measurements of singly ionized helium RRLs can also be used to assess the performance of the GBT/ACS spectrometer. Helium RRLs are typically ~10% the intensity of hydrogen RRLs from Galactic H II regions and PNe. Here we use our He and H RRL measurements to calculate the ^{4}He$^+$/H$^+$ ratio, y_4^+. For a more accurate determination of y_4^+, we use the integrated intensity of the RRL transitions:

$$y_4^+ = \frac{T_{\rm pk}({\rm He}) \times \Delta V({\rm He})}{T_{\rm pk}({\rm H}) \times \Delta V({\rm H})}, \qquad (1)$$

where the line peaks, $T_{\rm pk}$, and FWHM line widths, ΔV, are the values from the Gaussian fits to the observed spectra that are listed in Appendix A. Figure 7 plots these y_4^+ ratios for our PN sample as a function of the He RRL peak intensity, $T_{\rm pk}$(He). Because of the intrinsic weakness of the He emission, y_4^+ can only be derived from our GBT observations for $\Delta N \leqslant 4$ transitions. The error bars shown are $\pm 1\sigma$ errors of the Gaussian fits. The large difference in source integration time

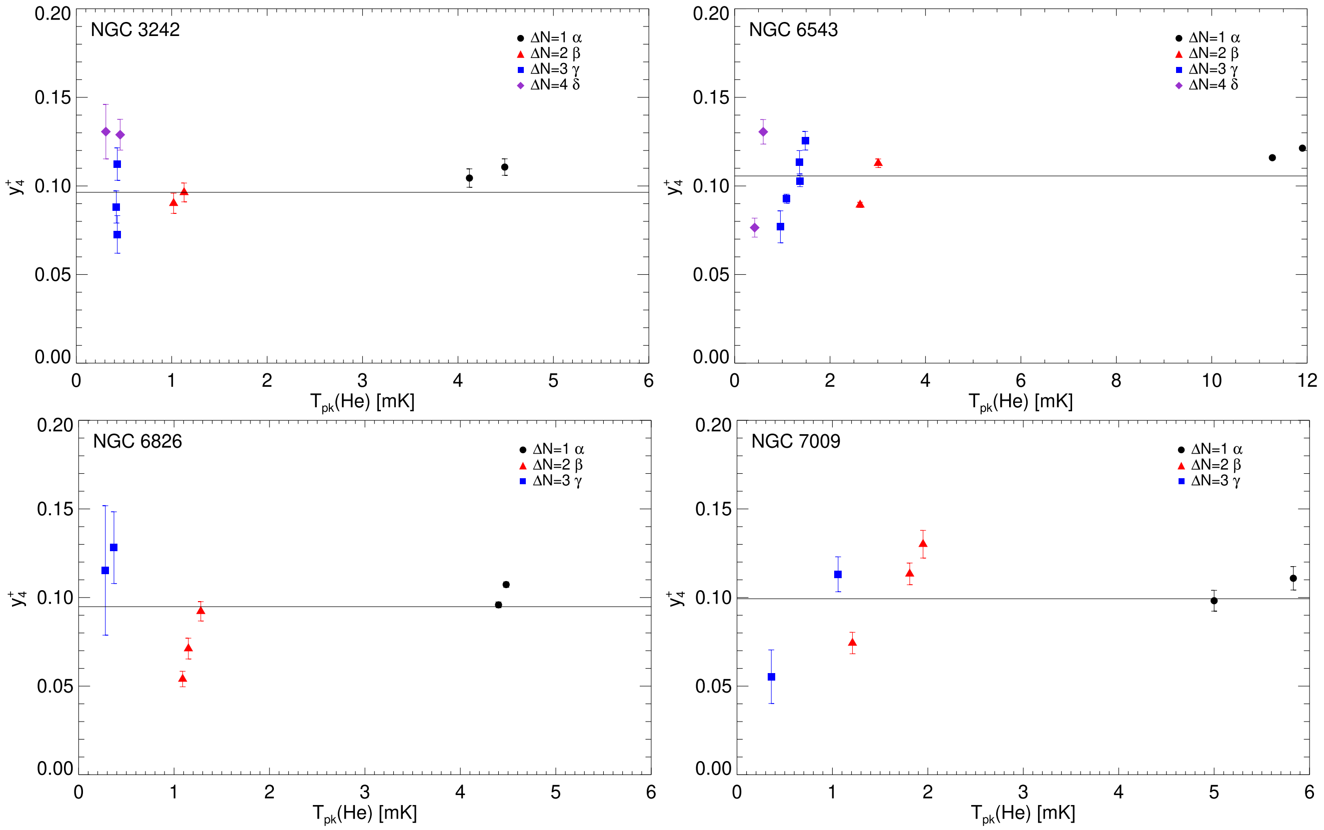

Figure 7. The ^{4}He$^+$/ H$^+$ ratio, y_4^+, derived for our sample PNe plotted as a function of the He RRL intensity, $T_{\rm pk}$(He). Horizontal lines show the weighted average of the α, β, and γ transitions. Error bars stem from $\pm 1\sigma$ errors of Gaussian fits to the observed RRLs.

between NGC 3242/NGC 6543 and NGC 6826/NGC 7009 is clearly seen. The poorer spectral sensitivity for NGC 6826/NGC 7009 means that He RRL emission cannot be detected for transitions beyond $\Delta N = 3$.

The horizontal lines in Figure 7 show the error-weighted y_4^+ average of the α, β, and γ transitions. For our PN sample targets, y_4^+ is nominally ∼0.10. This y_4^+ value gives us another metric with which to assess the performance of the GBT/ACS spectrometer. It tells us that every H RRL ought to have a corresponding He line with ∼10% the intensity of the hydrogen transition. This is a very important metric because it allows us to interpret what is *not* plotted in Figure 7 in the context of instrumental baseline frequency structure. Specifically, there are observed spectra that ought to show He RRL detections but do not. That we cannot see these lines means that they are being masked by BN.

It is clear from Figure 7 that at the ∼ few milliKelvin level for the He RRL intensity, we do not measure the same y_4^+ to within the formal errors. For example, our NGC 3242 observations have sufficient sensitivity to robustly detect He RRLs beyond the $\Delta N = 2$ β transitions. The H RRL intensities predict that, for $y_4^+ \sim 0.1$, the He RRLs ought to have intensities of ∼0.5 and ∼0.2 mK for the γ and δ transitions. These predictions are not reliably confirmed. The NGC 3242 RRL data (see Appendix A) show that we detect He γ emission at the appropriate ∼0.5 mK level for the 130, 131, and 132 transition spectra, but not for the 130a/130b spectra. Furthermore, although we have nominal He RRL detections for the 144b, 144g, and 145δ transition spectra, the measured He intensities differ by nearly a factor of 3 and the inferred y_4^+ values are ∼0.13, which is 30% above the nominal y_4^+ value.

From all these tests, we conclude that our ability to measure accurate spectral line parameters with the GBT/ACS spectrometer system for the integration times achieved here becomes compromised by instrumental baseline frequency structure—BN—effects at antenna temperatures $\lesssim$1–2 mK. Our GBT/ACS data show that we can detect RRLs at these intensities, but the measured line parameters, $T_{\rm pk}$ and ΔV, are uncertain by as much as ∼50% due to BN.

5. Radio Recombination Line Emission from Planetary Nebulae

We can use our measured RRL parameters to assess various global physical properties of our PNe sample. Our spectra are extremely sensitive. The NGC 3242 and NGC 6543 data in particular have integration times spanning ∼200 to ∼ 300 hr. Below we discuss the ^{4}He$^+$/H$^+$, y_4^+, abundances, FWHM spectral line widths, and excitation state of the PN sample as a whole.

5.1. ^{4}He$^+$ Abundance

We cannot characterize the ionization state of our sample PNe based solely on the GBT RRL spectra reported here. Our GBT data give no observational constraints on either the ^{4}He/H or ^{4}He^{++}/H$^+$ abundances. We can, however, use our RRL observations to assess the ^{4}He$^+$/H$^+$ abundance ratio of our PN sample sources. The central exiting stars of PNe have very high effective temperatures, $T_{\rm eff} \approx 100{,}000$ K (Osterbrock & Ferland 2006), and these high temperatures are indeed

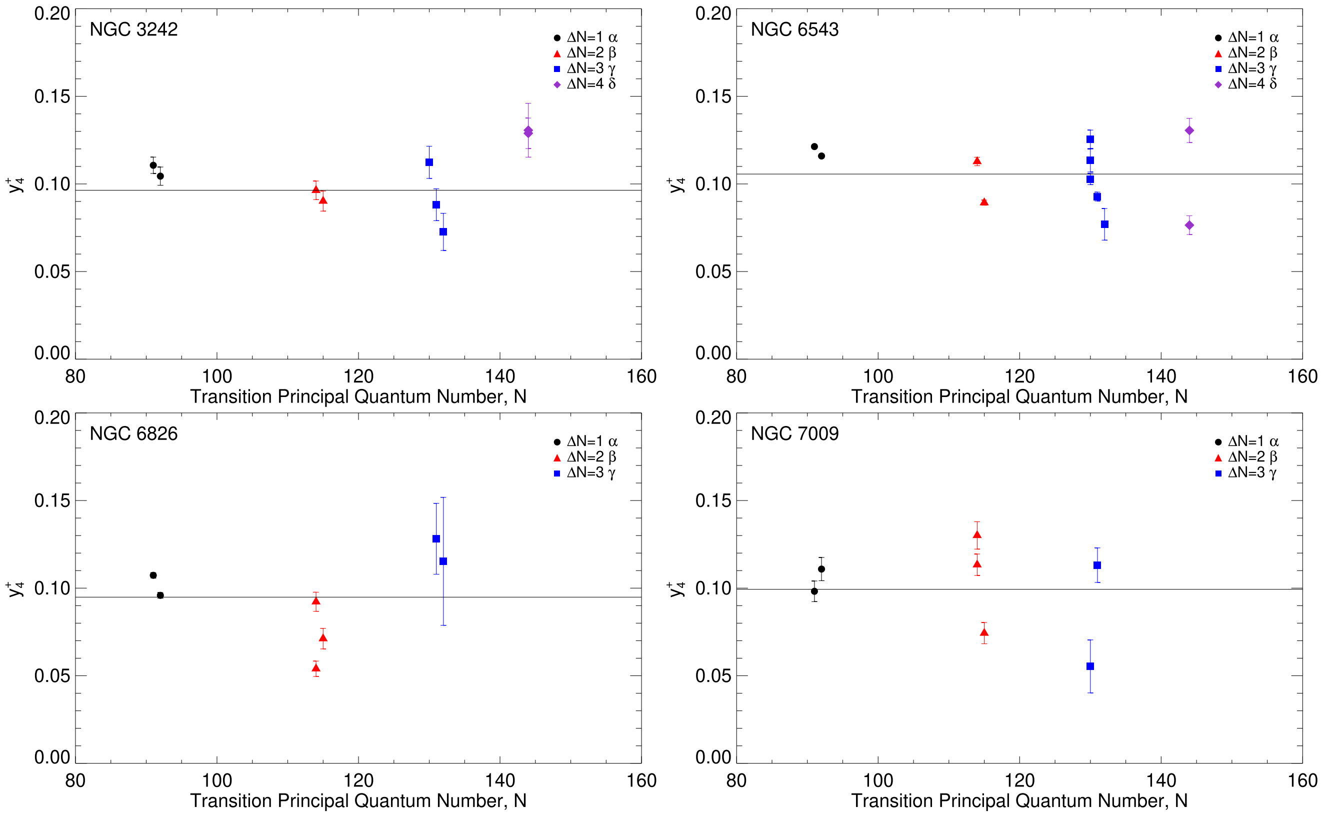

Figure 8. Observed RRL ^{4}He$^+$/H$^+$ ratio, y_4^+, for the planetary nebula sample as a function of transition principal quantum number, N. For sources with the largest integration times, we can detect He RRL emission from transitions with quantum number changes of $\Delta N = 4$. The horizontal lines show the average y_4^+ ratio for the α, β, and γ transitions. Error bars are $\pm 1\sigma$ and stem from Gaussian fits to the spectra. We find $y_4^+ \sim 0.10$ for our PNe sample.

present in our PNe sample (see Table 1). One thus expects very high ionization states near these stars. This corresponds to the inset regions shown in Figure 1. What ionization state we actually measure is complicated because approximately 80% of the Gaussian GBT beam area is sampling only halo gas, not these inner regions. This sampling bias is counterbalanced, however, by the fact that the RRL emission-line intensities scale as the local electron density squared so the RRL emission from these nebulae overwhelmingly stems from their dense, inner regions.

Thus, given the large GBT beam, our RRL observations provide only a global characterization of the ^{4}He$^+$/H$^+$ abundance of the combination of the PN cores plus their halos. Figure 8 shows the ^{4}He$^+$/H$^+$, y_4^+, abundances for our PNe plotted as a function of transition principal quantum number, N. The y_4^+ values are calculated using Equation (1) for each valid He/H RRL measurement pair and the abundance for each principal quantum number is determined by the average of all pairs at each N weighted by the spectral integration time. The horizontal lines in the figure are the error-weighted averages of the α, β, and γ transitions.

The RRL-based y_4^+ abundances for our sample PNe are characterized by $y_4^+ \sim 0.10$. Constructing detailed models of PNe requires high-resolution optical data to constrain the complex ionization structure of these sources. In Section 6 below we craft numerical models for NGC 3242 and NGC 6543. There we specify the He ionization state of these nebulae using ^{4}He optical recombination lines. The optical and radio ^{4}He$^+$/H$^+$ abundances are roughly consistent for both NGC 3242 (Table 6) and NGC 6543 (Table 7). The NGC 3242 model, for example, shows that its RRL emission arises almost entirely from its inner double shell—the inset image region in Figure 1—and that RRL emission from the halo is negligible.

5.2. Line Widths

The RRL line widths that we measure result from a combination of many physical processes. Broadening mechanisms include thermal motions, nonthermal motions (i.e., turbulence), bulk expansion, other types of velocity gradients along the line of sight, and pressure broadening. As discussed above, the GBT's substantial centimeter-wavelength beam size, ∼87″, complicates the interpretation of the line widths. The widths that we measure are a complex combination of the properties of both the PN inner cores and their extended halos. Our RRL FWHM line width measurements for our PN sample are summarized in Figure 9, which plots the line width as a function of the transition change in principal quantum number, ΔN. The line widths measured for all of the RRL transitions with the same ΔN were averaged weighted by their spectral integration time to give the FWHM values used in Figure 9.

For each PN in our sample, its Gaussian FWHM line width does not significantly change with ΔN. We thus appear to see no obvious evidence for pressure broadening whose effects should appear at high ΔNs (or, equivalently, Ns). But von Procházka et al. (2010) analyzed the line shapes of RRL spectra observed for the H II region Sgr B2(N). Their transitions spanned a large range of N and thus ought to show pressure-broadening effects and they do. For their analysis, they fit Voigt, Gaussian, and Lorentzian line shapes to their spectra.

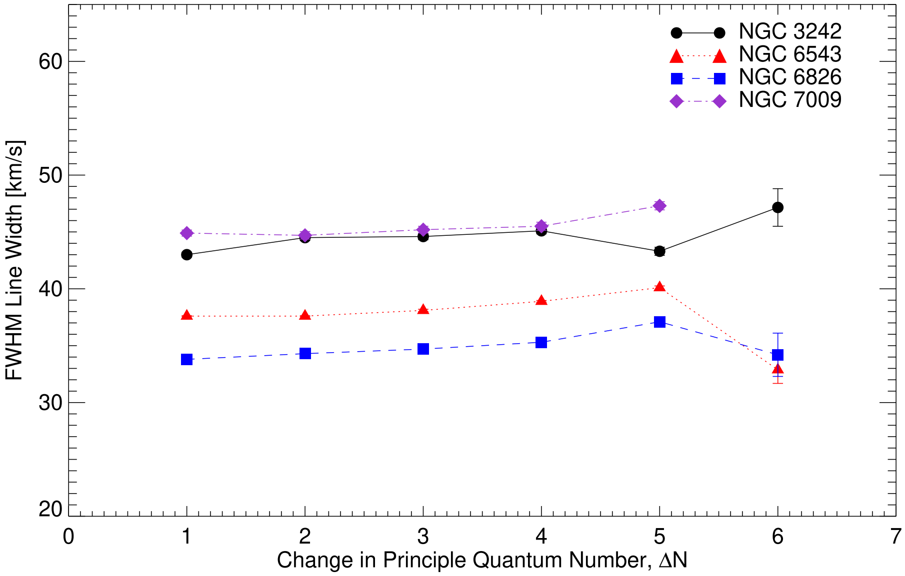

Figure 9. Observed RRL FWHM line widths for our sample PNe plotted as a function of the transition's change in principal quantum number, ΔN. The error bars are $\pm 1.5\sigma$ and stem from the Gaussian fits to the spectra. The significant expansion velocities of the plasma surrounding our PNe are clearly seen in their line widths.

Their Figure 1 shows that the FWHMs for these different line shapes are essentially identical.

The FWHM of an RRL is thus not a useful indicator of pressure broadening. The effects of pressure broadening are only apparent in the extended line wings or in the peak emission. Our RRL sensitivity is too poor for us to be able to make any reliable fits to the spectral line wings, but we do have the sensitivity to detect pressure broadening in the line peak emission (see Sections 5.3 and 6.2).

The expansion of the nebular gas surrounding our sample PNe, however, is clearly seen in their ~35–45 km s^{-1} line widths. Both PNe and H II regions are fully ionized plasmas produced by the ionizing radiation from their exciting stars. The majority of Galactic H II regions do not have substantial expansion velocities. Our PNe line widths thus are ~10–20 km s^{-1} larger than the average Galactic H II region FWHM line width of 25 km s^{-1}(Wenger et al. 2019b). Most of this line broadening must be due to expansion. It certainly is not due to temperature effects because the plasma electron temperatures of Galactic H II regions and our sample PNe are almost identical. Using the H91α and continuum measurements, we can derive electron temperatures, $T_{\rm e}$, for our PN sample's plasmas from these observed line-to-continuum ratios. We find $T_{\rm e}$ spanning the range ~7000 to ~13,000 K. These temperatures are typical values for Galactic H II regions (see Wenger et al. 2019a for the $T_{\rm e}$ derivation and typical H II region temperatures).

Table 5
RRL Oscillator Strengths and LTE Intensity Ratios

Transition	N	ΔN	$f_{\rm NM}$	LTE Ratio
H91α	91	1	0.1764667825E+02	1.00000
H114β	114	2	0.3080855700E+01	0.27399
H130γ	130	3	0.1090205890E+01	0.12608
H144δ	144	4	0.5237520000E+00	0.07432
H154ϵ	154	5	0.2926137750E+00	0.04749
H164ζ	164	6	0.1831153100E+00	0.03370
H171η	171	7	0.1218369570E+00	0.02438
H180θ	180	8	0.8682048000E−01	0.01925
H187ι	187	9	0.6395970050E−01	0.01531
H193κ	193	10	0.4854865600E−01	0.01238
H198λ	198	11	0.3773162250E−01	0.01012
H203μ	203	12	0.3002285000E−01	0.00847
H208ν	208	13	0.2436411250E−01	0.00721
H213ξ	213	14	0.2010511620E−01	0.00624
H221o	221	15	0.1704013000E−01	0.00570
H222π	222	16	0.1420736100E−01	0.00479
H227ρ	227	17	0.1217512075E−01	0.00429
H232σ	232	18	0.1053422930E−01	0.00388
H236τ	236	19	0.9157915750E−02	0.00349
H238υ	238	20	0.7964236400E−02	0.00309
H239ϕ	239	21	0.6950849150E−02	0.00272
H247χ	247	22	0.6263460000E−02	0.00261
H249ψ	249	23	0.5554700550E−02	0.00236
H249ω	249	24	0.4918615500E−02	0.00209

Note. LTE ratio = transition/H91α.

5.3. Intensities and Excitation

To what extent can our PN excitation states be described by local thermodynamic equilibrium (LTE)? To make this assessment, we need to know the expected LTE ratio between an (N,ΔN) transition and a fiducial (N,$\Delta N = 1$) transition. Our observations dictate our choices. We use H91α as the fiducial transition and calculate the LTE ratios expected for a set of our observed RRL transitions. We use the prescription in Menzel (1968) to derive the oscillator strengths, $f_{\rm NM}$, for recombination transitions between principal quantum numbers $N \rightarrow M$. Table 5 lists the oscillator strengths for some of the radio recombination line transitions observed here. The Table 5 transitions span order changes in principal quantum number, ΔN, between 1 and 24. Not all of these transitions were detected; we list this information here for completeness.

The LTE RRL intensity ratio between two optically thin transitions is given by the ratio of their oscillator strengths, $f_{\rm NM}/f'_{\rm NM}$, and their statistical weights, g_N/g'_N, where $g_N = 2 \times N^2$:

$$\text{LTE Intensity Ratio} = \frac{g_N \times f_{\rm NM}}{g'_N \times f'_{\rm NM}}. \qquad (2)$$

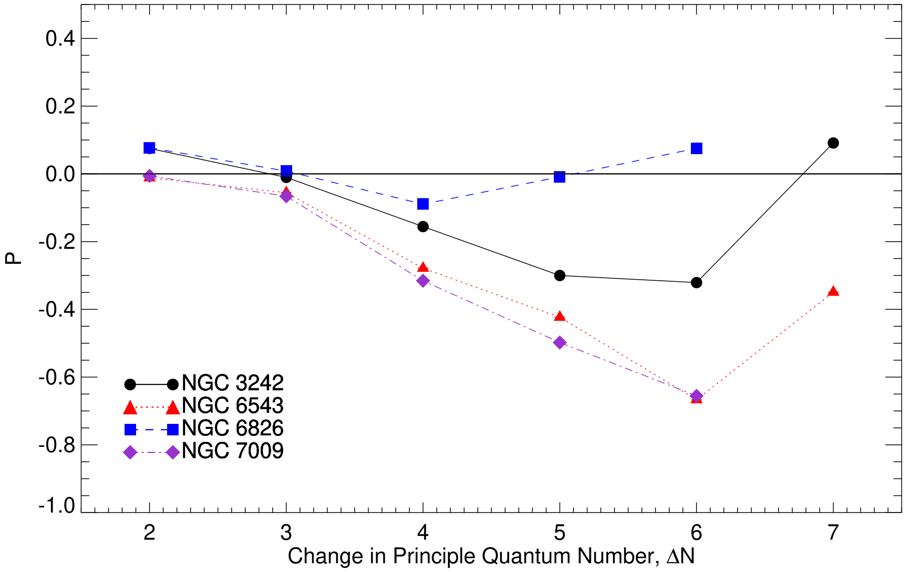

Figure 10. Comparison of the fractional difference between the observed line ratio and the LTE ratio as a function of the change in the transition principal quantum number, ΔN. Plotted here is the normalized fractional difference, $P = R - 1$, where R = observed ratio/LTE ratio. Each R ratio is that between the integrated intensity (mK km s^{-1}) of the RRL transition and the $\langle \mathrm{H}\alpha \rangle$ transition divided by the LTE ratio (see text). The $\pm 1\sigma$ error bars of these data are those of the Gaussian fits to the RRLs. These error bars are the size of the plotted symbols. For most of the PNe in our sample, apparent departures from LTE are seen with increasing ΔN. The RRL intensities at these high ΔN transitions, however, are quite weak, and their measurement accuracy is compromised by instrumental baseline frequency structure (see text Section 4).

The LTE intensity ratios between some of our observed transitions and H91α are listed in the final column of Table 5.

To make the LTE assessment, we use the observed integrated intensity of each RRL transition, $W_{\mathrm{RRL}} = T_{\mathrm{pk}} \times \Delta V$ (mK km s^{-1}), where the line peaks, T_{pk}, and FWHM line widths, ΔV, are the values from the Gaussian fits to the observed RRL spectra that are listed in Appendix A. Our observations include both measurements of adjacent N RRL transitions with the same ΔN as well as identical (N,ΔN) transitions sampled by different spectrometer SPWs. For each ΔN, we use here a single integrated intensity, $\langle W_{\Delta N} \rangle$, that is the average value of these multiple measurements weighted by the integration time of their spectra. In particular, the fiducial comparison transition we use is the weighted average of the H91α and H92α transitions, $\langle \mathrm{H}\alpha \rangle$.

All the PNe in our sample show apparent departures from LTE for $\Delta N > 3$. This can be seen in Figure 10, which compares the fractional difference between the observed line ratio and the LTE ratio as a function of the principal quantum number change, ΔN. Plotted is the normalized fractional difference, $P = R - 1$, where R = observed ratio/LTE ratio. Each R ratio is that between $\langle W_{\Delta N} \rangle$, the observed average ratio for a ΔN, and $\langle \mathrm{H}\alpha \rangle$, divided by the LTE ratio listed in Table 5. The $\pm 1\sigma$ error bars for Figure 10 stem from the Gaussian fits to the RRLs and are the size of the plotted symbols.

From the analysis in Section 4, however, we know that systematic instrumental frequency structure in the spectral baselines—the spectral BN—is compromising the RRL measurements for ~2 mK line intensities. Our ability to measure RRL parameters with the GBT/ACS spectrometer becomes increasingly inaccurate for $\Delta N \gtrsim 3$ transitions. The error bars in Figure 10 reflect only the error in the Gaussian fits to the RRLs. The precise magnitude of the BN for any particular RRL spectral region is unknown so the overall effect on this LTE analysis is uncertain. Given this, we deem that numerical modeling of our PN sources (see Section 6 below) provides a more robust means to assess any LTE effects.

Some of the apparent non-LTE behavior seen in Figure 10, however, is probably due to pressure broadening. We observe lower integrated intensities than expected by LTE for the higher ΔN transitions. The effects of pressure broadening are to diminish the line intensity and broaden the line wings as ΔN increases. But, as we discuss in Section 5.2, our FWHM line width measurements are insensitive to any broadening in the line wings. Therefore, the only pressure-broadening effect that would be apparent in our RRL data would be the drop in line intensity as ΔN increases. Pressure broadening would then manifest as a decrease in R and P as ΔN increases. At low ΔN, however, P would be ~0. This is consistent with Figure 10.

6. Planetary Nebula ^{3}He Abundances

The GBT ^{3}He$^+$ spectra for planetary nebulae reported here are more sensitive and have less instrumental baseline structure than any previously taken by the MPIfR 100 m and NRAO 140 Foot telescopes. We do not confirm the detection of ^{3}He$^+$ emission from NGC 3242 based on the independent observations made by those two telescope spectrometers. Apparently, systematic baseline frequency structure was an even bigger issue than we thought for these telescopes. Furthermore, we show in Section 4 that these effects are still an issue with the unblocked aperture GBT, albeit at a much lower spectral intensity.

Given the importance of the ^{3}He abundance in PNe, we derive the ^{3}He/H abundances for NGC 3242 and NGC 6543 as if the line parameters listed in Table 4 described actual detections. So here we determine upper limits for the ^{3}He/H abundances in these PNe. Because NGC 6826 and NGC 7009 have substantially poorer sensitivity, we choose not to calculate ^{3}He/H abundance upper limits for these sources.

To do this, we must determine the abundance of ^{3}He relative to H. This requires a model since the collisionally excited ^{3}He$^+$

Table 6
NEBULA Model Parameters for NGC 3242

Component	$V_{\rm exp}$ (km s^{-1})	Angular Size (arcsec)	$T_{\rm e}$ (K)	$n_{\rm e}$ (cm^{-3})	^{4}He$^+$/H$^+$	^{4}He^{++}/H$^+$	^{3}He$^+$/H$^+$
Inner Shell	20	10–25	13,000	2079	0.080	0.020	3.6×10^{-5}
Outer Shell	20	25–44	13,000	747	0.130	0.001	4.5×10^{-5}
Halo	11	44–120	13,000	10	0.100	0.000	4.5×10^{-5}

hyperfine line intensity depends on the density, whereas both the free–free continuum and RRL intensities are proportional to the density squared. The free–free thermal continuum intensity is used to derive the H abundance which is a critical step in the determination of the ^{3}He/H abundance ratio. An ionization correction is also necessary to convert the ^{3}He$^+$/H$^+$ abundance to a ^{3}He/H abundance ratio by number. We use a numerical code, NEBULA[7] (Balser & Bania 2018b), originally developed by Balser (1995), to model our sources and derive upper limits for their ^{3}He/H abundance ratios. Balser & Bania (2018a) used NEBULA to construct H II region models and they briefly describe the code but full details are found in Balser (1995).

A NEBULA model planetary nebula is composed solely of H and He within a three-dimensional Cartesian grid with arbitrary density, temperature, and ionization structure. Each numerical cell specifies values for the following quantities: electron temperature, $T_{\rm e}$, electron density, $n_{\rm e}$, ^{4}He$^+$/H$^+$ abundance ratio, ^{4}He^{++}/H$^+$ abundance ratio, and the ^{3}He$^+$/H$^+$ abundance ratio. The ^{3}He$^+$ transition is assumed to be in LTE, but non-LTE effects and pressure broadening from electron impacts can be included for the RRL modeling. All spectra are broadened by thermal and microturbulent motions. NEBULA calculates synthetic observations for ^{3}He$^+$, RRL, and continuum emission by performing the radiative transfer through the model grid. The radiative transfer is executed from the back of the grid to the front to produce the brightness distribution on the sky. To simulate an observation, NEBULA calculates model spectra by convolving this brightness distribution with a Gaussian beam that has the GBT's HPBW at the ^{3}He$^+$ frequency.

6.1. NGC 3242

We used NEBULA to model NGC 3242 in the past (see, e.g., Balser et al. 1997). The NEBULA model described here, however, supersedes all previous efforts. Much better PN information is now available to constrain the model and the GBT observations reported here are far superior to those taken previously by on-axis, blocked aperture telescopes.

The NEBULA model for NGC 3242 is comprised of a set of nested spheres with uniform properties. The model has a multishell morphology and a large halo (Phillips et al. 2009). The properties of the three nested, spherically symmetric shells are summarized in Table 6. We adopt the Gaia DR2 parallax distance listed in Table 1. The RRL emission arises primarily from the denser inner and outer shells, also called the "rim" and "shell" (Balick 1987). The angular extent of both these components is defined by observations and can be seen as the black circular inset core region of the Figure 1 NGC 3242 image. A significant portion of the ^{3}He$^+$ emission comes from the diffuse halo which entirely fills the GBT beam.

The kinematics of NGC 3242 are captured by the shape of spectral lines. These lines are primarily broadened by three mechanisms: expansion, thermal motions, and nonthermal motions. We assume a symmetric expanding nebula with a velocity that is constrained by optical collisionally excited lines (CELs) toward the center of the nebula (Weinberger 1989). The electron temperature (see below) determines the amount of thermal line broadening. Any nonthermal broadening, assumed to be constant throughout the nebula, is constrained by the observed line width of the RRLs.

The electron temperature, electron density, and He ionization structure is determined using both optical and radio data. The RRL-to-continuum ratio provides a good estimate for the electron temperature. Our GBT observations of the NGC 3242 H91α and continuum emission yield $T_{\rm e} = 12{,}700$ K, which is consistent with the optical integral-field spectroscopy value determined by Monteiro et al. (2013). The electron density that is predicted from optical CELs varies significantly depending on the tracer. We therefore adopt an average value based on data from Monteiro et al. (2013) for each component. These values are adjusted slightly to match the observed RRL peak intensities.

The He ionization structure adopted for our NGC 3242 model is summarized in Table 6. It is constrained by ^{4}He optical recombination lines (Monteiro et al. 2013). These observations directly measure the singly and doubly ionized He abundance ratios. Given the high electron temperature, we assume there is no neutral helium within NGC 3242 and that the ^{3}He ionization structure follows that of ^{4}He. We also adopt a halo abundance, y_4^+, of ^{4}He$^+$/H$^+ = 0.1$ and assume that the halo contains no doubly ionized ^{4}He. The y_4^+ value derived from our RRL data is between the optical y_4^+ values for the inner and outer shells (0.08 and 0.13, respectively). Because the RRL emission comes primarily from the shells and not the halo, the radio and optical data are roughly consistent. Using this ionization structure, we make an ionization correction to the NEBULA model input ^{3}He/H abundance: ^{3}He$^+$/H$^+$ = [^{4}He$^+$/H$^+$/^{4}He/H] × ^{3}He/H.

This NEBULA model does an excellent job in accounting for the continuum and RRL emission observed for NGC 3242. Altogether, 42 hydrogen and helium RRL transitions were calculated. NEBULA synthetic spectra are shown in Appendix B for eight representative transitions: H91α, ^{3}He$^+$, H114β, H115β, H130γ, H131γ, H144δ, and H152ϵ. Except for the 144δ H and He transitions, there is excellent agreement between the modeled and observed spectra. There is a well-known impedance mismatch in the GBT's *X*-band feed horn that produces a "suck out" at frequencies very near those of the 144δ H and He transitions that severely compromises the spectral baselines in that particular SPW.

6.2. NGC 6543

As with NGC 3242, we treat the ^{3}He$^+$ parameters listed in Table 4 for NGC 6543 as if this were an actual detection and use them to derive an upper limit for the ^{3}He/H abundance using a NEBULA model. Here, however, our model is overly simple. NGC 6543 is an extremely complex source. We deem it

---

[7] See http://ascl.net/1809.009.

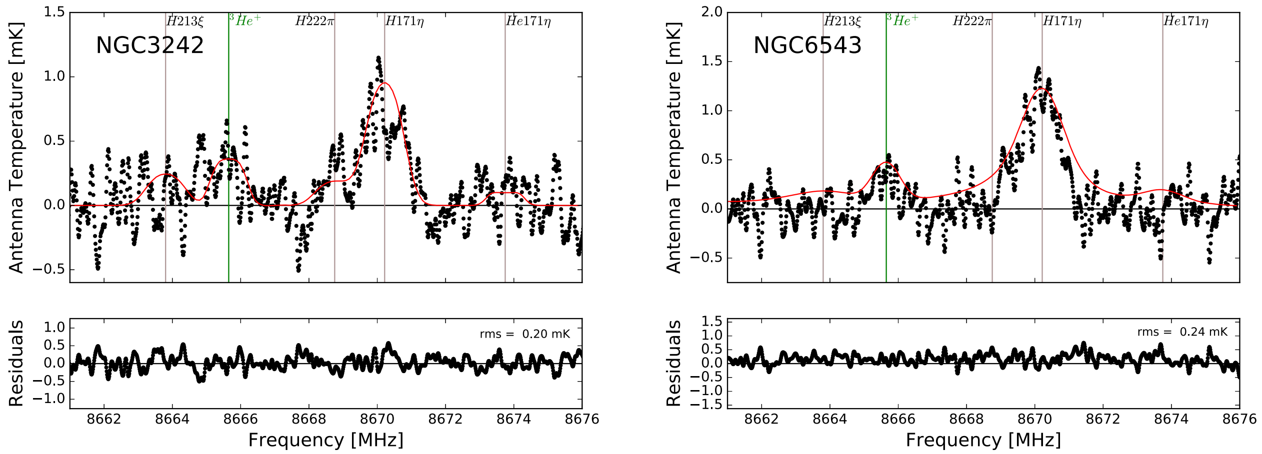

Figure 11. NGC 3242 and NGC 6543 NEBULA models for line emission in the ^{3}He$^+$ spectral band (red) compared with observations (black). The residuals between the observed spectra and the models are shown in the plots below the spectra. Vertical lines flag the recombination transitions present in each spectral band. These models set the upper limits for the ^{3}He/H abundances quoted here.

Table 7
NEBULA Model Parameters for NGC 6543

Component	$V_{\rm exp}$ (km s^{-1})	Angular Size (arcsec)	$T_{\rm e}$ (K)	$n_{\rm e}$ (cm^{-3})	^{4}He$^+$/H$^+$	^{4}He^{++}/H$^+$	^{3}He$^+$/H$^+$
Shell	17	9.2−19.4	8,000	3750	0.12	0.0	7.3×10^{-5}
Halo	10	19.4−165	14,700	35	0.12	0.0	7.3×10^{-5}

unnecessary to construct a more sophisticated model in order to derive what is a notional upper limit to the ^{3}He/H abundance.

The NEBULA model for NGC 6543 has an inner shell surrounded by a large halo. The properties of these two nested, spherically symmetric shells are summarized in Table 7. We adopt the Gaia DR2 parallax distance listed in Table 1. The angular extent of both model components is defined by observations. The RRL emission arises primarily from the denser inner shell, the "rim" (Balick & Hajian 2004). In order to better match the RRL spectra, we include non-LTE and pressure-broadening effects in the NEBULA model. As with NGC 3242, a significant portion of the ^{3}He$^+$ emission comes from the diffuse halo that entirely fills the GBT beam. We assume that both components exhibit symmetric expansion velocities and constrain them using optical CELs. For the shell, we adopt the rim velocity measured by Schönberner et al. (2014) using [O III]/[N II]. The halo expansion velocity, as well as all its other physical properties, is adopted from Middlemass et al. (1989).

The electron temperature and He ionization structure are constrained by both optical and radio data. The RRL-to-continuum ratio provides an estimate for the electron temperature. Our GBT observations of the NGC 6543 H91α and continuum emission yield $T_{\rm e} = 7300$ K. This is consistent with optical measurements (Hyung et al. 2001). We adopt the ionization structure derived by Bernard-Salas et al. (2003). This gives a y_4^+ of ^{4}He$^+$/ H$^+ = 0.12$. The model has no neutral or doubly ionized helium.

For NGC 6543, there is clear evidence of pressure broadening when comparing the NEBULA model RRL intensities with the GBT observations. To produce a reasonable NEBULA model requires that non-LTE/pressure-broadening effects together with a higher local density specified with a volume filling factor of 0.2 (Balser et al. 1999a) be included. This NGC 6543 NEBULA model also accounts for the observed continuum emission. The synthetic RRL spectra are shown in Appendix B for H91α, ^{3}He$^+$, H114β, H115β, H130γ, H131γ, H144δ, and H152ϵ. The model does a reasonable job in reproducing the RRL observations for low-order transitions. Its ability to reproduce the RRL spectra, however, clearly becomes problematic at the higher ΔN transitions.

6.3. Upper Limits to the ^{3}He Abundance in Planetary Nebulae

We have not detected ^{3}He$^+$ emission from any of our sample PNe so we can only set upper limits on the ^{3}He/H abundance ratio from these observations using our NEBULA models. To derive a ^{3}He abundance, a NEBULA model ^{3}He/H ratio is set so that the synthetic ^{3}He$^+$ hyperfine transition intensity is consistent with the observed spectrum. The ^{3}He$^+$ NEBULA model spectra for NGC 3242 and NGC 6543 are shown in Figure 11. We find that a ^{3}He abundance ratio of ^{3}He/H $= 4.5 \times 10^{-5}$ for NGC 3242 and 7.3×10^{-5} for NGC 6543 by number gives a reasonable approximation to the observed spectrum.

Here we did not attempt to fit the NEBULA ^{3}He abundance to the NGC 3242 and NGC 6543 spectra in any formal numerical way because each model takes many CPU hours to run. We are, after all, modeling an upper limit for these abundances. Furthermore, the NEBULA model for NGC 3242 is quite good and does an excellent job in accounting for the observed RRL and continuum emission. On the other hand, the NGC 6543 NEBULA model is really just a notional one. Our model is clearly too simple, even with the inclusion of non-LTE effects, pressure broadening, and clumping. We therefore deem that our NGC 6543 ^{3}He/H upper limit is not very reliable.

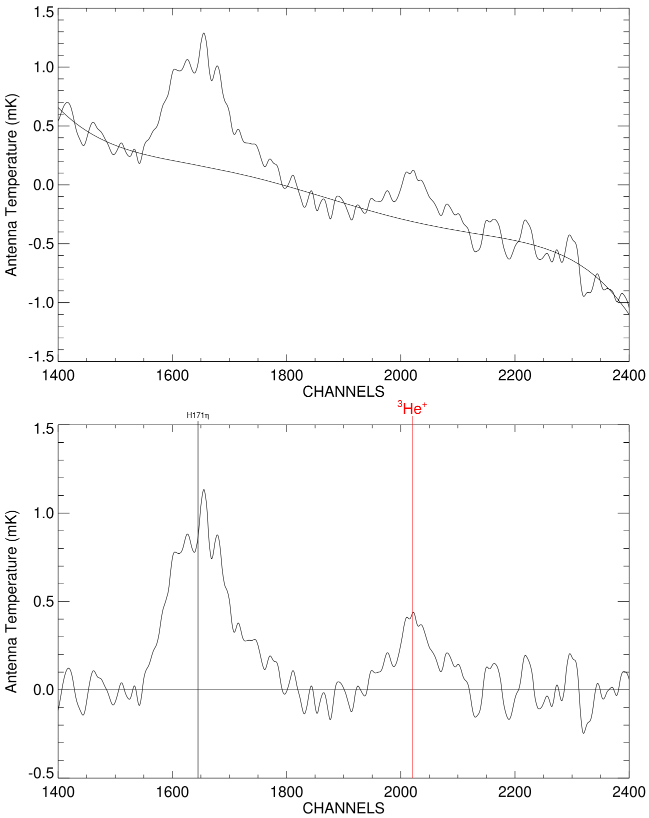

Figure 12. Composite average ^{3}He$^+$ spectrum for NGC 3242 and NGC 6543. The spectrum was smoothed to 5 km s^{-1} resolution. After smoothing, this 557.7 hr integration has 98 μK rms noise. Top: the fifth-order instrumental baseline fit is shown superimposed atop the data. Bottom: spectrum that results when this baseline model is subtracted. Vertical lines flag the locations of the H171η and ^{3}He$^+$ transitions.

7. Discussion

Our measurements of ^{3}He emission from Galactic H II regions and planetary nebulae are at the sensitivity limit of the GBT/ACS spectrometer. The RRL spectra show that this sensitivity is sufficient to robustly detect and to measure the properties of spectral lines that have $\gtrsim 1$ mK intensities and line widths of $\sim$25 km s^{-1}. Balser & Bania (2018a) analyzed the H II region ^{3}He sample. They found that the ^{3}He/H abundances of H II regions show a shallow negative gradient when plotted as a function of Galactic radius that is roughly consistent with the Lagarde et al. (2012) stellar evolution models that include thermohaline mixing.

Our ^{3}He/H upper limits, especially that for NGC 3242, support the extra-mixing solution to the "^{3}He Problem." Unfortunately, these results are still insufficient to prove that thermohaline mixing in particular occurs in all low-mass stars. Should ^{3}He be definitively detected in even one planetary nebula, its ^{3}He/H abundance would place significant constraints on extra-mixing processes in low-mass stars and, in turn, models for stellar evolution and Galactic chemical evolution. A high ^{3}He/H abundance ratio derived for even a single PN would indicate that some mechanism must be at play to inhibit the extra-mixing in this object. Extra-mixing should otherwise occur in all low-mass stars.

7.1. Has ^{3}He$^+$ Emission Been Detected in Any Planetary Nebula?

We have not made any reliable detections of ^{3}He$^+$ emission from our PN sample objects with our GBT/ACS observations. In particular, we can only set an upper limit on the ^{3}He/H abundance in NGC 3242, thus failing to confirm previously reported detections of ^{3}He$^+$ emission based on observations made with the NRAO 140 Foot and MPIfR 100 m telescopes. It is therefore reasonable to ask whether ^{3}He$^+$ emission has been detected from any planetary nebula. Two other PNe have published ^{3}He$^+$ detections: IC 418 and J 320.

7.1.1. IC 418

Using the NASA Deep Space Station 63 (DSS-63) telescope, Guzman-Ramirez et al. (2016) report the detection of ^{3}He$^+$ emission from the PN IC 418. The lack of any serious tests of the DSS-63 spectral baselines, however, together with large discrepancies in the observed RRL line parameters make this claimed detection highly suspect. From their Table 1, the measured α and β RRL transition intensities differ by 7% and 14%, respectively. Furthermore, the ^{4}He$^+$/H$^+$ ratios reported are 0.112, 0.037, 0.258, 0.095, and 0.117 for the 91α, 92α, 114β, 115β, and 116β transitions, respectively. The intensities and line ratios should be the same for these transitions within the errors. Also compare the variation in their y_4^+ values with those reported here for our PN sample. These are systematic errors in the Guzman-Ramirez et al. (2016) measurements hidden in plain sight. From this, we judge that the level of instrumentally caused systematic uncertainty in the DSS-63 data is at least $\sim$5 mK, making their reported $\sim$10 mK ^{3}He$^+$ detection a $\sim 2\sigma$ signal.

7.1.2. J 320

The advantage of interferometers like the NRAO Very Large Array (VLA) is that much, but not all, of the instrumental baseline structure is correlated out. We therefore deem that the Balser et al. (2006) ^{3}He$^+$ detection for J 320 with the VLA is more robust than that reported for any other PN. The signal-to-noise ratio (S/N) is only 4, but when averaging over a halo region, the S/N increases to 9. Nevertheless, the J 320 VLA observations suffer from three problems: (1) a 3.3 MHz ripple caused by reflections within the waveguide (common to all antennas), (2) a limited number of channels and bandwidth which together provide only a very small spectral region with which to determine the instrumental baseline, and (3) only one RRL transition to assess the accuracy of the measurements. The latter two deficiencies are due to the capabilities of the VLA correlator.

The next step in the study of ^{3}He production in PNe is to confirm the J 320 detection. We plan to use the enhanced VLA, the Jansky Very Large Array (JVLA) to do this. The JVLA overcomes all three problems with the VLA observations (Perley et al. 2011). Optical fiber has replaced the old waveguides and the 3.3 MHz ripple is no longer present. The new Wideband Interferometric Digital ARchitecture (WIDAR) correlator provides an ample number of channels across a large bandwidth to measure the spectral baseline accurately. Finally, the flexibility of WIDAR allows one to tune to many RRLs simultaneously. This will provide the data needed to carefully assess the quality of the spectral baselines.

7.2. PN Composite Spectrum

A composite ^{3}He$^+$ spectrum that is the average of our NGC 3242 and NGC 6543 observations is shown in Figure 12. It was processed in an identical manner to that for individual PN

Table 8
Stellar Model ^{3}He Yields[a]

Stellar Mass $M_\odot$	Mixing Process	Y_3 $\times 10^{-4}$
1.00	standard	6.39
	thermohaline	1.35
	thermohaline + rotation	1.50
1.25	standard[b]	...
	thermohaline	1.96
	thermohaline + rotation	2.04

Notes.
[a] Mass fraction ^{3}He yields, Y_3, from Lagarde et al. (2011) stellar evolution models.
[b] No standard mixing model calculated.

spectra. This spectrum nearly doubles the integration time of the ^{3}He$^+$ spectral band. After smoothing to 5 km s^{-1} resolution, this 557.7 hr integration has 98 μK rms noise and a quality factor, Q, of 1.60. Figure 12 shows the spectral baseline and its model before subtraction. Even with existing spectrometer systems such as the GBT/ACS, this composite ^{3}He$^+$ spectrum suggests that given sufficiently large integration times robust detections of ^{3}He$^+$ emission from planetary nebulae can be made.

We cannot construct a NEBULA model for this composite spectrum, which also means that a ^{3}He/H abundance cannot be derived. The Figure 12 spectrum does give an estimate for the sensitivity required to detect ^{3}He$^+$ emission from PNe. Nonetheless, the ^{3}He/H abundances derived for such extremely weak ^{3}He$^+$ emission from individual PN will imply that there is little if any net production of ^{3}He in low-mass stars.

7.3. Mixing Processes in Low-mass Stars

Can our upper limits for the ^{3}He/H abundance in PNe still provide any insight about mixing mechanisms in low-mass stars? Lagarde et al. (2011) make specific predictions for ^{3}He production by such stars from various mixing processes. They calculate a grid of stellar models and report the ^{3}He produced during main-sequence stellar evolution as a mass fraction yield, Y_3. Lagarde et al. (2011) find that the ^{3}He yields depend on stellar mass and metallicity. We deem our most robust ^{3}He/H upper limit abundance is that for NGC 3242. Galli et al. (1997) cite a mass of 1.2 ± 0.2 $M_\odot$ for the NGC 3242 progenitor star which has a mass fraction metallicity $Z = Z_\odot/2 = 0.0061$ (Barker 1985) where the Sun's metallicity, $Z_\odot$, is 0.0122 (Asplund et al. 2006a, 2006b). This NGC 3242 metallicity is closest to the Lagarde et al. (2011) models listed in their Table 3 where $Z = 0.004$. Their ^{3}He model yields for various mixing mechanisms are summarized in Table 8.

Our GBT upper limit for NGC 3242 is ^{3}He/H $< 4.5 \times 10^{-5}$ by number. Because the stellar yields are given as mass fractions, this abundance ratio must be converted to mass fraction, Y_3:

$$Y_3 = \frac{3\, y_3(1 - Z)}{1 + 4y} < 9.6 \times 10^{-5}, \qquad (3)$$

where y_3 is the ^{3}He abundance ratio upper limit, ^{3}He/H; y is the ^{4}He abundance ratio, ^{4}He/H = 0.1 (Monteiro et al. 2013); and Z is the heavy element mass fraction. (Details of this conversion of number density to mass fraction are given in Appendix C.)

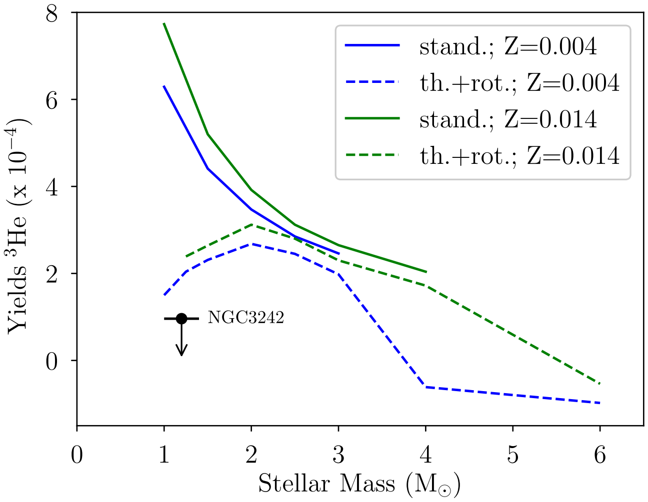

Figure 13. Comparison of our ^{3}He mass fraction upper limit for NGC 3242 with the Lagarde et al. (2011) stellar evolution models. The model Y_3 yields are adopted from their Figure 9. The models shown have a range of metallicities, Z, and employ either standard mixing or a combination of thermohaline and rotational mixing.

Our ^{3}He mass fraction upper limit for NGC 3242 is compared in Figure 13 with the Lagarde et al. (2011) stellar evolution models. The model Y_3 yields are adopted from their Figure 9. The models shown have a range of metallicities, Z, and employ either standard mixing or a combination of thermohaline and rotational mixing. Because we derive here only a notional upper limit for the NGC 6543 ^{3}He/H abundance, its Y_3 limit is too unreliable to include in Figure 13.

It is clear that this NGC 3242 ^{3}He/H upper limit is inconsistent with standard stellar production of ^{3}He. The limit thus requires that some type of extra-mixing process operates in low-mass stars. This is now in conflict with Palla et al. (2002), who derive a ^{12}C/^{13}C abundance ratio limit for NGC 3242 that is consistent with standard stellar mixing yields. Their result is based on Hubble Space Telescope observations of the C [III] multiplet near 1908 Å wavelength.

Thermohaline mixing is currently the best model that is broadly consistent with our ^{3}He observations, but open questions remain. Our upper limit on Y_3 for NGC 3242 is in fact lower than all the Lagarde et al. (2011) model yields summarized in Table 8 including thermohaline mixing. One issue with thermohaline mixing models is in determining a value for the coefficient C, which is related to the aspect ratio of the mixing fingers (length/width). This is effectively a free parameter that must be estimated. Charbonnel & Lagarde (2010) use $C = 1000$, which is adopted from Charbonnel & Zahn (2007b). This produces abundance ratios that are consistent with observations in stars (e.g., their ^{12}C/^{13}C abundances). But models using lower values of C will not solve the ^{3}He problem (see Cantiello & Langer 2010). Hydrodynamic models are not consistent with $C \sim 1000$, but there are possible solutions (see Denissenkov & Merryfield 2011). Finally, the interplay between thermohaline and rotation-induced mixing may be important (see Maeder et al. 2013). Sengupta & Garaud (2018), for example, studied the effects of rotation on the thermohaline instability and found that rotation could in some cases significantly increase its mixing efficiency.

8. Summary

The ^{3}He abundance in H II regions and PNe provides important constraints for BBN, stellar evolution, and Galactic evolution. Standard stellar evolution models that predict the production of copious amounts of ^{3}He in low-mass stars, consistent with the high ^{3}He/H abundance ratios previously reported for a few planetary nebulae, are at odds with the approximately primordial values determined for Galactic H II regions. This inconsistency is called the "^{3}He Problem." Models that include mixing from the thermohaline instability and rotation provide mechanisms that reduce the enhanced ^{3}He/H abundances dredged up during the RGB stage. These models give ^{3}He yields that predict modest ^{3}He production by stars over the lifetime of the Milky Way and can reconcile the "^{3}He Problem."

Attempting to detect ^{3}He$^+$ in PNe challenges the capabilities of all existing radio spectrometer systems. Systematic instrumental baseline frequency structure compromises the ability of these spectrometer systems to measure the wide, weak ^{3}He$^+$ emission lines from PNe accurately. We previously reported detections of ^{3}He$^+$ emission from NGC 3242 made independently with the MPIfR 100 m and NRAO 140 Foot telescopes. The GBT observations discussed here do not confirm these results. Furthermore, our analysis calls into question all previously reported detections of ^{3}He$^+$ emission from planetary nebulae, save perhaps for J 320.

We derive upper limits for the ^{3}He/H abundance by number of $<4.5 \times 10^{-5}$ and $<7.3 \times 10^{-5}$ for the PNe NGC 3242 and NGC 6543, respectively. These are well below previously reported determinations and also well below the abundances predicted by standard stellar evolution theory. In fact, they approach the abundances found for the "The 3-Helium Plateau" defined by H II region ^{3}He/H abundances.

We dedicate this paper to our late colleague Bob Rood, whose seminal 1976 paper with Gary Steigman and Beatrice Tinsley led to the formation of our ^{3}He research team. We thank the GBT telescope operators whose diligence and expertise in executing our observing scripts during Semester 11A were exceptional. Bruce Balick and Nazar Budaiev helped prepare some figures. This research was partially supported by NSF award AST-1714688 to T.M.B.

Facility: GBT.

Software: TMBIDL (Bania et al. 2016), NEBULA (Balser & Bania 2018b).

Appendix A
Planetary Nebula Radio Recombination Line Parameters

The RRL parameters for the sample of Galactic PNe measured using Gaussian fits to observations made with the Green Bank Telescope near 8665 GHz are summarized in Tables 9–12. Compiled here for each nebula is the RRL transition, the change in principal quantum number, ΔN, the line intensity, $T_{\rm L}$, in mK, and the FWHM line width, ΔV in km s^{-1}, together with the rms noise in mK and integration time, $t_{\rm intg}$ in hr, of the spectral band containing the transition. Also listed are the 1σ errors of the Gaussian fits to the intensity, $\sigma T_{\rm L}$, and line width, $\sigma \Delta V$. Some transitions (H114a/H114b, H130a/H130b, and H144b/H144g) appeared in multiple spectral bands. These transitions were fit independently and are listed here for completeness.

Table 9
NGC 3242 Recombination Line Parameters

Transition	ΔN	$T_{\rm L}$ (mK)	$\sigma T_{\rm L}$ (mK)	ΔV (km s^{-1})	$\sigma \Delta V$ (km s^{-1})	rms (mK)	$t_{\rm intg}$ (hr)
H91	1	37.84	0.11	43.0	0.15	0.117	306.7
He91	1	4.49	0.12	40.1	1.30	0.117	306.7
H92	1	37.05	0.12	44.5	0.17	0.313	93.2
He92	1	4.12	0.13	41.8	1.60	0.313	93.2
H114	2	10.86	0.04	44.6	0.19	0.150	308.0
He114	2	1.13	0.04	41.3	1.73	0.150	308.0
H115	2	10.58	0.04	45.1	0.18	0.156	305.0
He115	2	1.02	0.04	42.2	2.09	0.156	305.0
H130	3	4.80	0.02	43.3	0.24	0.116	308.0
He130	3	0.43	0.02	54.3	3.63	0.116	308.0
H130a	3	5.15	0.04	45.4	0.42	0.238	91.7
H130b	3	5.24	0.03	45.0	0.32	0.228	94.4
H131	3	4.47	0.02	42.0	0.26	0.159	286.1
He131	3	0.42	0.03	39.4	2.91	0.159	286.1
H132	3	4.10	0.03	43.6	0.43	0.251	91.8
He132	3	0.43	0.04	30.2	3.38	0.251	91.8
H144b	4	2.30	0.02	42.4	0.38	0.116	305.0
He144b	4	0.31	0.02	41.1	4.01	0.116	305.0
H144g	4	2.33	0.02	43.8	0.34	0.107	286.1
He144g	4	0.46	0.02	28.6	1.44	0.107	286.1
H145	4	2.55	0.04	47.4	0.87	0.264	91.8
He145	4	0.80	0.04	51.4	3.18	0.264	91.8
H152	5	1.50	0.01	50.9	0.60	0.117	208.7
H154	5	0.84	0.16	22.9	4.90	0.117	306.7
H155	5	1.74	0.01	45.3	0.45	0.175	305.0
H156	5	1.75	0.03	47.0	1.20	0.263	91.8
H164	6	0.77	0.01	45.9	1.14	0.144	286.1
H165	6	0.86	0.04	51.0	2.81	0.231	93.2
H171	7	0.75	0.02	57.9	1.52	0.145	301.7

Table 10
NGC 6543 Recombination Line Parameters

Transition	ΔN	$T_{\rm L}$ (mK)	$\sigma T_{\rm L}$ (mK)	ΔV (km s^{-1})	$\sigma \Delta V$ (km s^{-1})	rms (mK)	$t_{\rm intg}$ (hr)
H91	1	92.08	0.06	37.6	0.03	0.146	258.1
He91	1	11.90	0.06	35.3	0.20	0.146	258.1
H92	1	90.22	0.06	37.6	0.03	0.326	65.7
He92	1	11.27	0.06	34.9	0.22	0.326	65.7
H114	2	24.72	0.04	38.1	0.07	0.151	263.5
He114	2	3.01	0.04	35.3	0.59	0.151	263.5
H115	2	23.77	0.02	38.9	0.05	0.173	257.3
He115	2	2.63	0.03	31.4	0.38	0.173	257.3
H130	3	10.47	0.02	40.1	0.10	0.168	263.9
He130	3	1.37	0.03	31.5	0.68	0.168	263.9
H130a	3	9.90	0.03	37.4	0.14	0.278	65.9
He130a	3	1.48	0.04	31.4	0.99	0.219	65.9
H130b	3	9.99	0.04	38.3	0.18	0.311	65.1
He130b	3	1.36	0.05	31.9	1.41	0.311	65.1
H131	3	10.17	0.02	41.7	0.08	0.139	236.2
He131	3	1.09	0.02	36.1	0.73	0.139	236.2
H132	3	9.91	0.06	39.4	0.26	0.386	53.4
He132	3	0.96	0.07	31.3	2.86	0.386	53.4
H144b	4	4.86	0.02	38.3	0.18	0.166	257.3
He144b	4	0.60	0.02	40.5	1.65	0.166	257.3
H144g	4	4.98	0.02	40.8	0.15	0.166	236.2
He144g	4	0.42	0.02	37.0	1.89	0.166	236.2
H145	4	3.61	0.08	30.2	0.82	0.403	53.4
H152	5	3.08	0.02	47.4	0.37	0.158	191.6
H154	5	2.07	0.06	30.4	1.05	0.146	258.1
H155	5	2.51	0.02	41.4	0.35	0.192	257.3
H156	5	1.76	0.06	31.9	1.27	0.307	53.4
H164	6	1.13	0.03	31.4	0.91	0.188	236.2
H165	6	1.35	0.05	38.2	1.66	0.315	65.7
H171	7	1.13	0.01	48.4	0.78	0.112	256.1

Table 11
NGC 6826 Recombination Line Parameters

Transition	ΔN	$T_{\rm L}$ (mK)	$\sigma T_{\rm L}$ (mK)	ΔV (km s^{-1})	$\sigma \Delta V$ (km s^{-1})	rms (mK)	$t_{\rm intg}$ (hr)
H91	1	37.18	0.04	33.8	0.04	0.255	51.6
He91	1	4.48	0.04	30.1	0.33	0.255	51.6
H92	1	36.53	0.04	34.3	0.04	0.394	51.1
He92	1	4.40	0.05	27.3	0.34	0.394	51.1
H114a	2	10.48	0.04	34.7	0.15	0.345	51.5
He114a	2	1.28	0.05	26.2	1.16	0.345	51.5
H114b	2	10.58	0.04	35.3	0.16	0.331	51.4
He114b	2	1.09	0.06	18.5	1.10	0.331	51.4
H115	2	10.06	0.04	37.1	0.19	0.296	51.4
He115	2	1.15	0.06	23.1	1.47	0.296	51.4
H130a	3	4.57	0.04	35.9	0.37	0.296	51.5
H130b	3	4.72	0.04	36.6	0.34	0.292	51.4
H131	3	3.81	0.04	38.8	0.47	0.350	48.1
He131	3	0.37	0.04	51.2	5.83	0.350	48.1
H132	3	4.05	0.05	37.0	0.56	0.342	43.1
He132	3	0.28	0.07	61.7	11.95	0.342	43.1
H144b	4	2.25	0.04	38.6	0.70	0.336	51.4
H144g	4	2.24	0.04	37.0	0.72	0.351	48.1
H154	5	1.41	0.04	34.5	1.25	0.255	51.6
H155	5	1.36	0.04	43.3	1.35	0.304	51.4
H156	5	1.78	0.05	40.4	1.61	0.315	43.1
H164	6	1.33	0.04	34.2	1.27	0.366	48.1

Table 12
NGC 7009 Recombination Line Parameters

Transition	ΔN	$T_{\rm L}$ (mK)	$\sigma T_{\rm L}$ (mK)	ΔV (km s^{-1})	$\sigma \Delta V$ (km s^{-1})	rms (mK)	$t_{\rm intg}$ (hr)
H91	1	50.24	0.18	44.9	0.18	0.232	47.2
He91	1	5.00	0.18	44.3	2.11	0.232	47.2
H92	1	50.70	0.22	44.7	0.22	0.398	46.8
He92	1	5.83	0.22	43.1	1.98	0.398	46.8
H114a	2	13.46	0.05	45.2	0.20	0.318	44.1
He114a	2	1.81	0.06	38.1	1.61	0.318	44.1
H114b	2	13.54	0.06	45.5	0.24	0.312	43.9
He114b	2	1.95	0.07	41.1	1.96	0.312	43.9
H115	2	13.15	0.06	47.3	0.24	0.336	47.2
He115	2	1.21	0.06	38.2	2.46	0.336	47.2
H130a	3	5.96	0.05	46.4	0.47	0.390	44.1
He130a	3	0.36	0.06	42.5	9.19	0.390	44.1
H130b	3	6.09	0.04	45.6	0.34	0.358	43.9
H131	3	5.96	0.05	44.5	0.41	0.411	45.4
He131	3	1.06	0.06	28.3	1.84	0.411	45.4
H132	3	5.09	0.04	47.5	0.48	0.447	39.7
H144b	4	2.48	0.05	45.1	1.02	0.348	47.2
H144g	4	2.30	0.05	41.1	1.03	0.402	45.4
H145	4	2.51	0.05	57.3	1.54	0.789	39.7
H154	5	0.78	0.21	30.7	9.68	0.232	47.2
H155	5	1.54	0.04	47.1	1.39	0.402	47.2
H156	5	1.67	0.07	46.4	2.66	0.352	39.7
H164	6	1.21	0.08	21.7	1.56	0.304	45.4

Appendix B
NEBULA Model Spectra for Radio Recombination Lines

Representative model RRL spectra for the PNe NGC 3242 and NGC 6543 compared with the GBT observations are shown in Figures 14–17. These NEBULA models are described in Section 6 and their properties summarized in Tables 6 and 7, respectively. The black circles are the observed spectra whereas the red lines are the NEBULA model spectra. The residuals between the data and the models are shown in the plots below the spectra. The recombination transitions present in each spectral band are flagged with vertical lines.

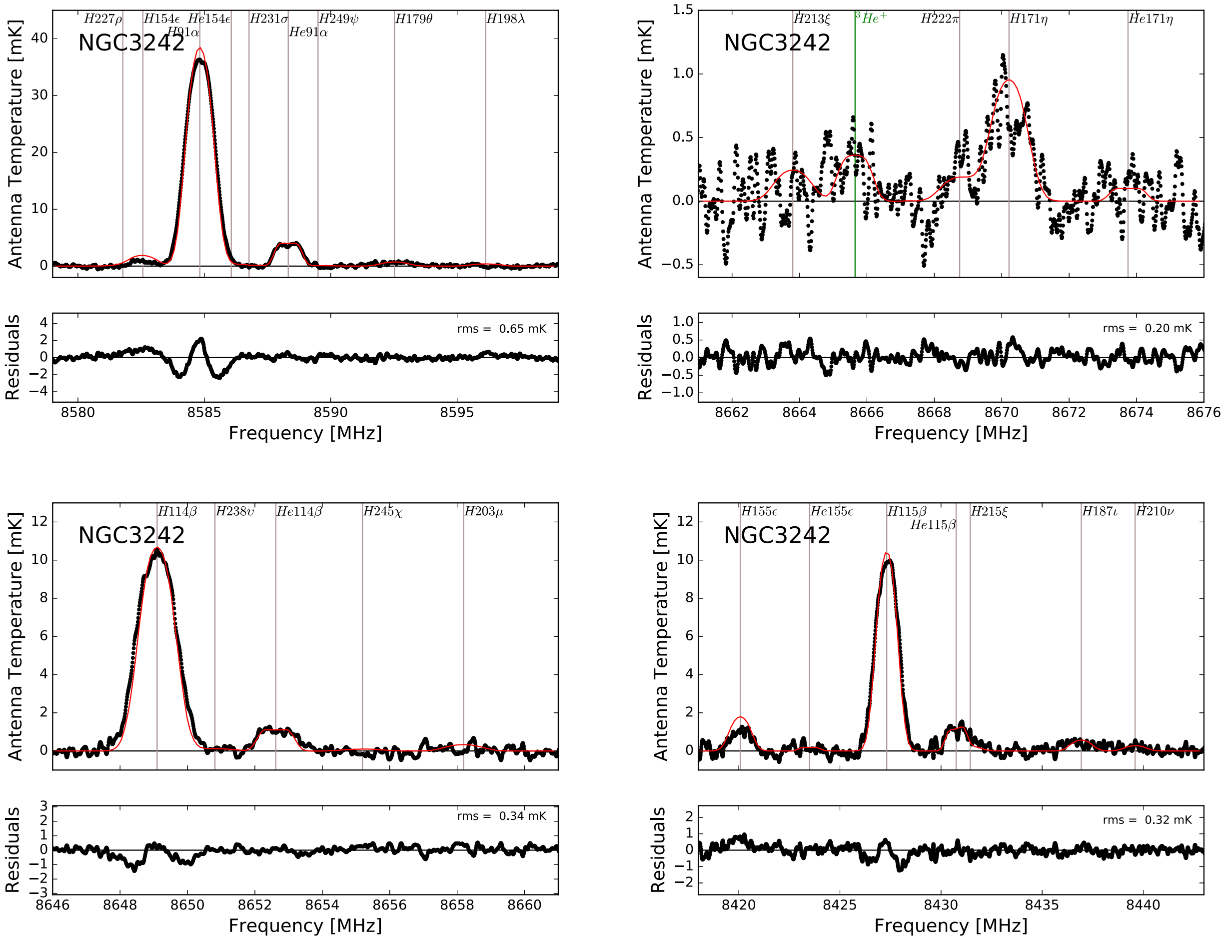

Figure 14. NGC 3242 NEBULA models. Starting at the top left, the following spectral bands were modeled: H91α, ^{3}He$^+$, H114β, and H115β.

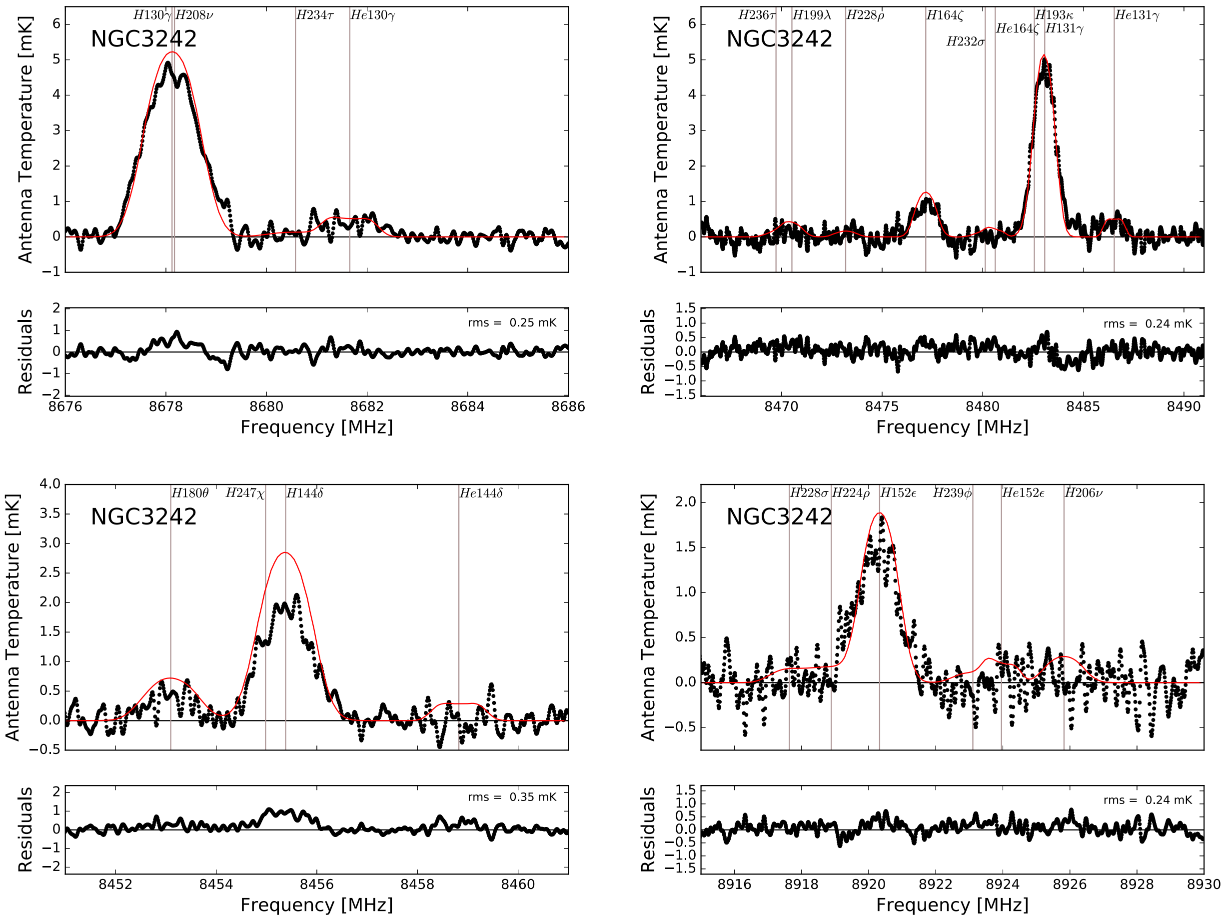

Figure 15. NGC 3242 NEBULA models. Starting at the top left, the following spectral bands were modeled: H130γ, H131γ, H144δ, and H152ϵ.

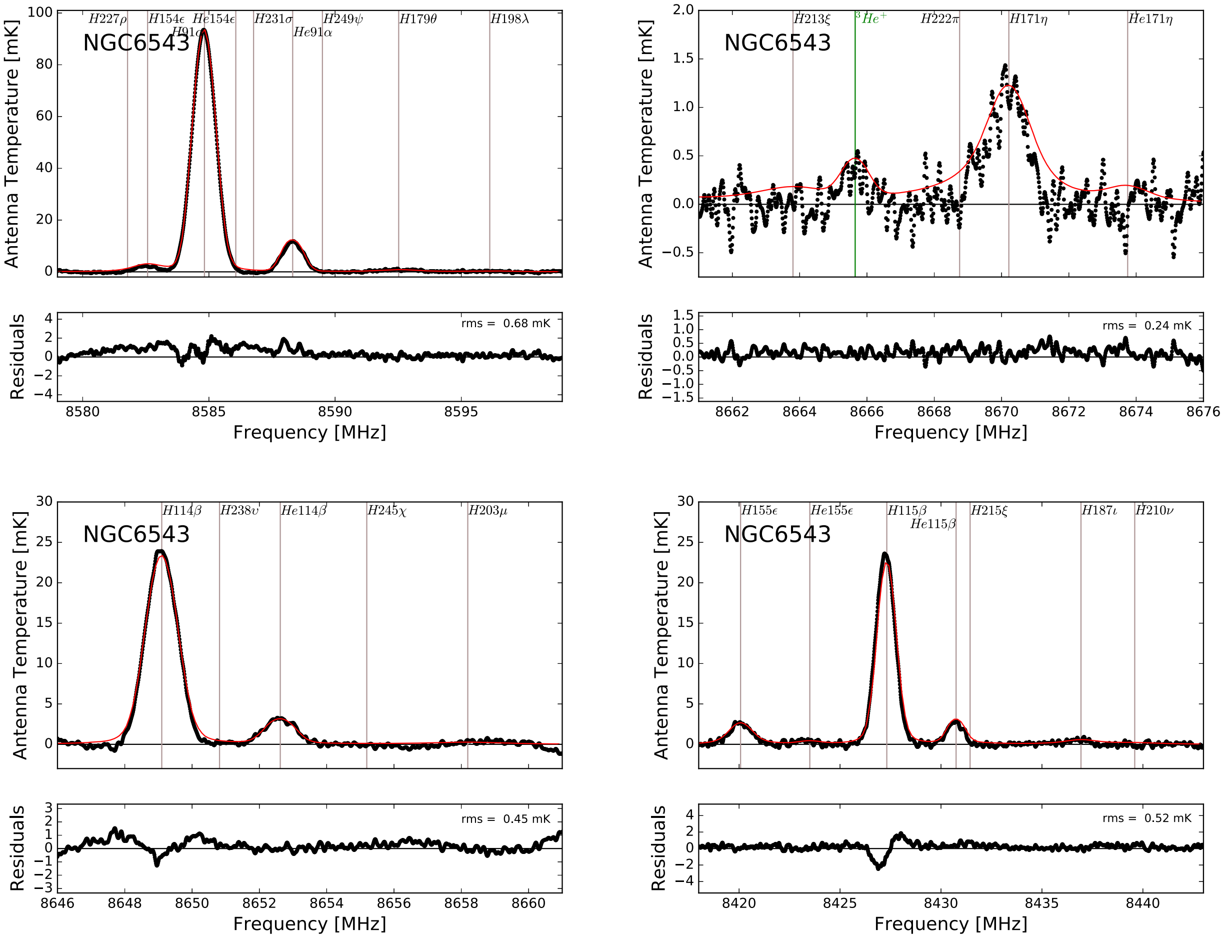

Figure 16. NGC 6543 NEBULA models. Starting at the top left, the following spectral bands were modeled: H91α, ^{3}He$^+$, H114β, and H115β.

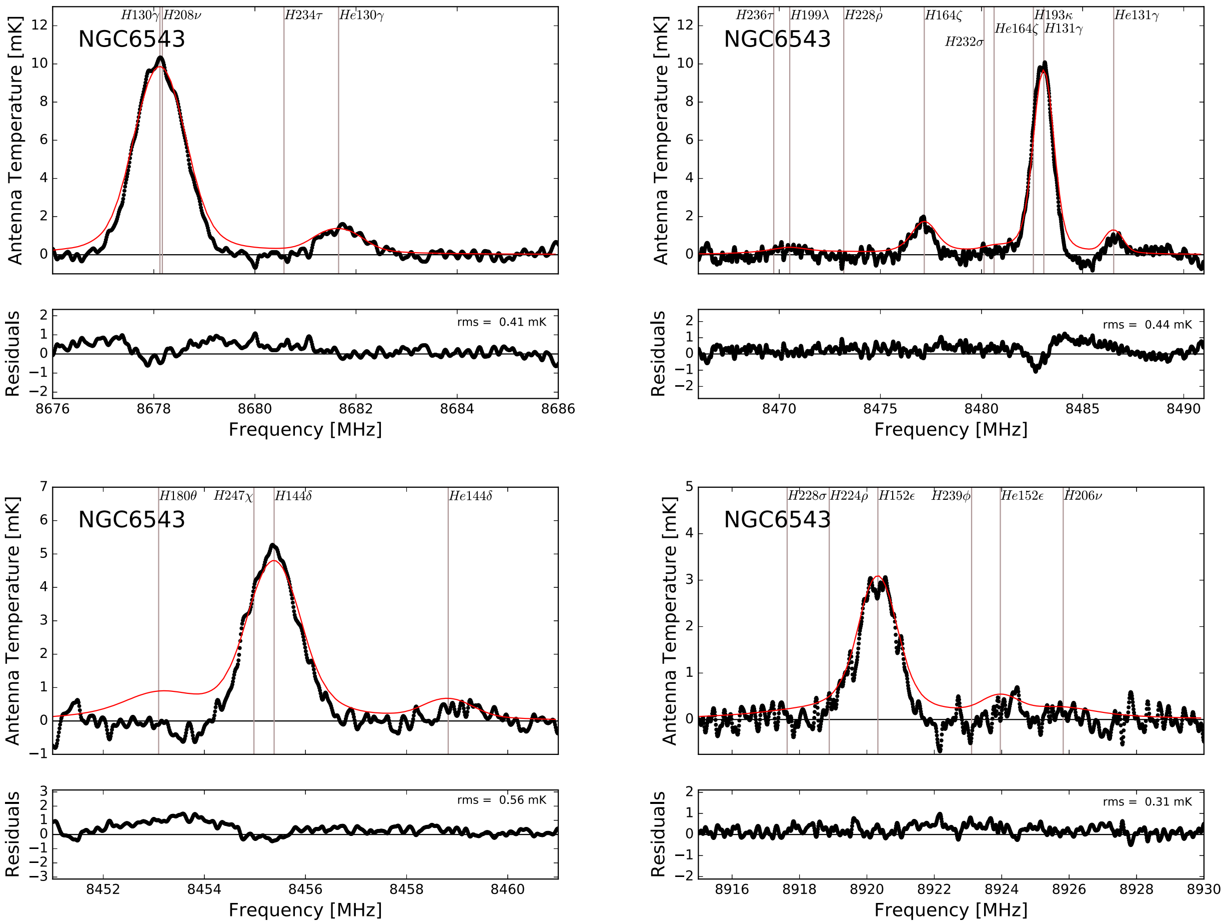

Figure 17. NGC 6543 NEBULA models. Starting at the top left, the following spectral bands were modeled: H130γ, H131γ, H144δ, and H152ϵ.

Appendix C
Conversion of Number Density to Mass Fraction

Abundance ratios are typically expressed either by number or by mass. The number density of species i is given by

$$n_i = \frac{X_i\,\rho}{m_i}, \tag{C1}$$

where ρ is the total density, $X_{\rm i}$ is the mass fraction of species i, and $m_{\rm i}$ is the mass of species i. We define X, Y, and Z to be the mass fraction of hydrogen, helium, and metals, respectively. Therefore, $X + Y + Z = 1$.

C.1. ^{4}He Abundances

From Equation (C1),

$$n(^4{\rm He}) = \frac{X(^4{\rm He})\rho}{m(^4{\rm He})} = \frac{Y\ \rho}{m(^4{\rm He})} \tag{C2}$$

and

$$n({\rm H}) = \frac{X({\rm H})\rho}{m({\rm H})} = \frac{X\ \rho}{m({\rm H})}. \tag{C3}$$

Therefore, the ^{4}He/H abundance ratio by number is given by

$$n(^4{\rm He})/n({\rm H}) \equiv y = \frac{Y\ m({\rm H})}{X\ m(^4{\rm He})}. \tag{C4}$$

But $X = 1 - Y - Z$ and $m(^4{\rm He}) \sim 4\,m({\rm H})$, so

$$y = \frac{Y}{4(1 - Y - Z)}. \tag{C5}$$

Solving for Y yields

$$Y = \frac{4\,y(1 - Z)}{(1 + 4y)}. \tag{C6}$$

Here we ignore nuclear binding energy and neglect the contribution of the less abundant isotopic abundances.

C.2. ^{3}He Abundances

From Equation (C1),

$$n(^3{\rm He}) = \frac{X(^3{\rm He})\rho}{m(^3{\rm He})} = \frac{Y_3\ \rho}{m(^3{\rm He})}, \tag{C7}$$

where we have defined the ^{3}He mass fraction as Y_3. Therefore, the ^{3}He/H abundance ratio by number is given by

$$n(^3{\rm He})/n({\rm H}) \equiv y_3 = \frac{Y_3\ m({\rm H})}{X\ m(^3{\rm He})}. \tag{C8}$$

But $X = 1 - Y - Z$ and $m(^3{\rm He}) \sim 3\,m({\rm H})$, so

$$y_3 = \frac{Y_3}{3(1 - Y - Z)}. \tag{C9}$$

Solving for Y_3 yields

$$Y_3 = 3\,y_3(1 - Y - Z). \tag{C10}$$

Substituting Y from Equation (C6) and rearranging terms yields

$$Y_3 = \frac{3\,y_3(1 - Z)}{1 + 4y}. \tag{C11}$$

ORCID iDs

T. M. Bania https://orcid.org/0000-0003-4866-460X
Dana S. Balser https://orcid.org/0000-0002-2465-7803

References

Asplund, M., Grevesse, N., & Jacques Sauval, A. 2006a, NuPhA, 777, 1
Asplund, M., Grevesse, N., & Sauval, A. J. 2006b, CoAst, 147, 76
Balick, B. 1987, AJ, 94, 671
Balick, B., & Hajian, A. R. 2004, AJ, 127, 2269
Balser, D. S. 1995, PhD thesis, Boston Univ.
Balser, D. S., & Bania, T. M. 2018a, AJ, 156, 280
Balser, D. S., & Bania, T. M. 2018b, NEBULA: Radiative Transfer Code of Ionized Nebulae at Radio Wavelengths, Astrophysics Source Code Library, ascl:1809.009
Balser, D. S., Bania, T. M., Brockway, C. J., Rood, R. T., & Wilson, T. L. 1994, ApJ, 430, 667
Balser, D. S., Bania, T. M., Rood, R. T., & Wilson, T. L. 1997, ApJ, 483, 320
Balser, D. S., Bania, T. M., Rood, R. T., & Wilson, T. L. 1999a, ApJ, 510, 759
Balser, D. S., Goss, W. M., Bania, T. M., & Rood, R. T. 2006, ApJ, 640, 360
Balser, D. S., Rood, R. T., & Bania, T. M. 1999b, ApJL, 522, L73
Bania, T., Wenger, T., Balser, D., & Anderson, L. 2016, TMBIDL: Single Dish Radio Astronomy Data Reduction Package, v8.1, Astrophysics Source Code Library, ascl:1605.005
Bania, T. M., Rood, R. T., & Balser, D. S. 2002, Natur, 415, 54
Bania, T. M., Rood, R. T., & Balser, D. S. 2007, SSRv, 130, 53
Barker, T. 1985, ApJ, 294, 193
Bernard-Salas, J., Pottasch, S. R., Wesselius, P. R., & Feibelman, W. A. 2003, A&A, 406, 165
Cantiello, M., & Langer, N. 2010, A&A, 521, A9
Charbonnel, C. 1995, ApJL, 453, L41
Charbonnel, C., & Lagarde, N. 2010, A&A, 522, A10
Charbonnel, C., & Zahn, J. P. 2007a, A&A, 476, L29
Charbonnel, C., & Zahn, J. P. 2007b, A&A, 467, L15
Chiappini, C., Renda, A., & Matteucci, F. 2002, A&A, 395, 789
Cyburt, R. H. 2004, PhRvD, 70, 023505
Denissenkov, P. A., & Merryfield, W. J. 2011, ApJL, 727, L8
Faulkner, D. J. 1970, ApJ, 162, 513
Fisher, J. R., Norrod, R. D., & Balser, D. S. 2003, NRAO Electronics Division Internal Rep. No. 312
Galli, D., Palla, F., Ferrini, F., & Penco, U. 1995, ApJ, 443, 536
Galli, D., Stanghellini, L., Tosi, M., & Palla, F. 1997, ApJ, 477, 218
Geiss, J. 1993, in Origin and Evolution of the Elements, ed. N. Prantzos, E. Vangioni-Flam, & M. Casse (Cambridge: Cambridge Univ. Press), 89
Gigho, F., Maddalena, R., Balser, D. S., & Langston, G. 2001, GBT Commissioning Memo, 10
Gloeckler, G., & Geiss, J. 1996, Natur, 381, 210
Greisen, E. W., Calabretta, M. R., Valdes, F. G., & Allen, S. L. 2006, A&A, 446, 747
Guzman-Ramirez, L., Rizzo, J. R., Zijlstra, A. A., et al. 2016, MNRAS, 460, L35
Hyung, S., Mellema, G., Lee, S. J., & Kim, H. 2001, A&A, 378, 587
Iben, I. J. 1967a, ApJ, 147, 650
Iben, I. J. 1967b, ApJ, 147, 624
Lagarde, N., Charbonnel, C., Decressin, T., & Hagelberg, J. 2011, A&A, 536, A28
Lagarde, N., Romano, D., Charbonnel, C., et al. 2012, A&A, 542, A62
Maeder, A., Meynet, G., Lagarde, N., & Charbonnel, C. 2013, A&A, 553, A1
Markwardt, C. B. 2009, in ASP Conf. Ser. 411, Astronomical Data Analysis Software and Systems XVIII, ed. D. A. Bohlender, D. Durand, & P. Dowler (San Francisco, CA: ASP), 251
Menzel, D. H. 1968, Natur, 218, 756
Middlemass, D., Clegg, R. E. S., & Walsh, J. R. 1989, MNRAS, 239, 1
Monteiro, H., Gonçalves, D. R., Leal-Ferreira, M. L., & Corradi, R. L. M. 2013, A&A, 560, A102
Osterbrock, D. E., & Ferland, G. J. 2006, Astrophysics of Gaseous Nebulae and Active Galactic Nuclei (2nd ed.; Mill Valley, CA: Univ. Science Books)
Palla, F., Bachiller, R., Stanghellini, L., Tosi, M., & Galli, D. 2000, A&A, 355, 69
Palla, F., Galli, D., Marconi, A., Stanghellini, L., & Tosi, M. 2002, ApJL, 568, L57
Peng, B., Kraus, A., Krichbaum, T. P., & Witzel, A. 2000, A&AS, 145, 1
Perley, R. A., Chandler, C. J., Butler, B. J., & Wrobel, J. M. 2011, ApJL, 739, L1
Phillips, J. P., Ramos-Larios, G., Schröder, K. P., & Contreras, J. L. V. 2009, MNRAS, 399, 1126
Ramos-Larios, G., Santamaría, E., Guerrero, M. A., et al. 2016, MNRAS, 462, 610
Romano, D., Tosi, M., Matteucci, F., & Chiappini, C. 2003, MNRAS, 346, 295
Rood, R. T. 1972, ApJ, 177, 681
Rood, R. T., Bania, T. M., & Wilson, T. L. 1984, ApJ, 280, 629
Rood, R. T., Bania, T. M., & Wilson, T. L. 1992, Natur, 355, 618
Rood, R. T., Steigman, G., & Tinsley, B. M. 1976, ApJL, 207, L57
Rood, R. T., Wilson, T. L., & Steigman, G. 1979, ApJL, 227, L97
Schönberner, D., Balick, B., & Jacob, R. 2018, A&A, 609, A126
Schönberner, D., Jacob, R., Lehmann, H., et al. 2014, AN, 335, 378
Schönberner, D., & Steffen, M. 2019, A&A, 625, A137
Sengupta, S., & Garaud, P. 2018, ApJ, 862, 136
Tosi, M. 1998, SSRv, 84, 207
von Procházka, A. A., Remijan, A. J., Balser, D. S., et al. 2010, PASP, 122, 354
Weinberger, R. 1989, A&AS, 78, 301
Wenger, T. V., Balser, D. S., Anderson, L. D., & Bania, T. M. 2019a, ApJ, 887, 114
Wenger, T. V., Dickey, J. M., Jordan, C. H., et al. 2019b, ApJS, 240, 24
Wilson, T. L., & Rood, R. 1994, ARA&A, 32, 191